Multiple Gravity Assists for Low Energy Transport in the Planar Circular Restricted 3-Body Problem

Matthew A. Werner

Thesis submitted to the Faculty of the
Virginia Polytechnic Institute and State University
in partial fulfillment of the requirements for the degree of

Master of Science
in
Aerospace Engineering

Shane D. Ross, Chair
Kevin K. Schroeder
Riley M. Fitzgerald

May 5, 2022
Blacksburg, Virginia

Keywords: Dynamical astronomy, symplectic maps, chaotic transport, resonances

Copyright 2022, Matthew A. Werner

Multiple Gravity Assists for Low Energy Transport in the Planar Circular Restricted 3-Body Problem

Matthew A. Werner

(ABSTRACT)

Much effort in recent times has been devoted to the study of low energy transport in multibody gravitational systems. Despite continuing advancements in computational abilities, such studies can often be demanding or time consuming in the three-body and four-body settings. In this work, the Hamiltonian describing the planar circular restricted three-body problem is rewritten for systems having small mass parameters, resulting in a 2D symplectic twist map describing the evolution of a particle's Keplerian motion following successive close approaches with the secondary. This map, like the true dynamics, admits resonances and other invariant structures in its phase space to be analyzed. Particularly, the map contains rotational invariant circles reminiscent of McGehee's invariant tori blocking transport in the true phase space, adding a new quantitative description to existing chaotic zone estimates about the secondary. Used in a patched three-body setting, the map also serves as a tool for investigating transfer trajectories connecting loose captures about one secondary to the other without any propulsion systems. Any identified initial conditions resulting in such a transfer could then serve as initial guesses to be iterated upon in the continuous system. In this work, the projection of the McGehee torus within the interior realm is identified and quantified, and a transfer from Earth to Venus is exemplified.

Multiple Gravity Assists for Low Energy Transport in the Planar Circular Restricted 3-Body Problem

Matthew A. Werner

(GENERAL AUDIENCE ABSTRACT)

The transport of a particle between celestial bodies, such as planets and moons, is an important phenomenon in astrodynamics. There are multiple ways to mediate this objective; commonly, the motion can be influenced directly via propulsion systems or, more exotically, by utilizing the passive dynamics admitted by the system (such as gravitational assists). Gravitational assists are traditionally modelled using two-body dynamics. That is, a spacecraft or particle performs a flyby within that body's sphere of influence where momentum is exchanged in the process. Doing so provides accurate and reliable results, but the design space effecting the desired outcome is limited when considering the space of *all* possibilities. Utilizing three-body dynamics, however, provides a significant improvement in the fidelity and variety of trajectories over the two-body approach, and thus a broader space through which to search. Through a series of approximations from the three-body problem, a discrete map describing the evolution of nearly Keplerian orbits through successive close encounters with the body is formed. These encounters occur outside of the body's sphere of influence and are thus uniquely formed from three-body dynamics. The map enables computation of a trajectory's fate (in terms of transit) over numerical integration and also provides a boundary for which transit is no longer possible. Both of these features are explored to develop an algorithm able to rapidly supply guesses of initial conditions for a transfer in higher fidelity models and further develop the existing literature on the chaotic zone surrounding the body.

Dedication

To my family, who have no idea what I do.

Acknowledgments

First and foremost, I would like to thank my advisor, Shane Ross, with my whole heart for his acceptance, patience, and guidance throughout my time in graduate school. I couldn't be more grateful to have been given the opportunity to work on this project and the things that followed from it. Another huge thank you goes out to Dr. Greg Earle, who also saw the potential in me and offered solid life and career advice when I needed it most.

I would also like to shout out my friends Jared van Dam, Jared Guzman, Max Weekly, Chase Leuchtmann, Arsam Jafaryzad, Jon Axmann, Rachel Bianculli, and many others for supporting me along the way. Finally to my friends of the Ross Dynamics Lab, thank you Albert Jarvis, Josh Fitzgerald, Manu Nimmala, and Emad Masroor for the laughs, insightful conversations, and wonderful memories throughout graduate school; I will always cherish the moments we had together.

Contents

List of Figures **viii**

List of Tables **xiv**

1 Introduction **1**

2 Dynamical models **3**

2.1 Continuous dynamics 4

2.1.1 The Hamiltonian 5

2.1.2 Jacobi's constant & Lagrange points 6

2.2 Small-body approximation 7

2.2.1 Decomposing the Hamiltonian 7

2.2.2 Tisserand's parameter & manifolds of the Lagrange points 9

2.3 Discrete dynamics 12

2.3.1 The Keplerian map 12

3 A boundary of chaotic transport **17**

3.1 Classifying trajectories 18

3.2 How to detect RICs 19

3.2.1 A method to identify RICs 22
3.3 Results 26
3.3.1 Comparison to other chaotic zones 29

4 Multibody transfer 31

4.1 Switching between systems 32
4.1.1 Preliminary energetic bounds 33
4.2 Symplecticity through reference orbits 35
4.2.1 Refining the energetic bounds 36
4.3 Finding transfer trajectories 38
4.3.1 Generating initial conditions 40
4.4 Demonstration of an uncontrolled transfer from Earth to Venus 41
4.4.1 Setup 41
4.4.2 Results 42

5 Conclusions 45

Bibliography 46

Appendices 49

Appendix A Transformation to Delaunay Variables for Orbital Elements 50

List of Figures

2.1 Approximating dynamically accurate trajectories as circular orbits (PCCR4BP). . 3

2.2 The PCR3BP in the rotating frame (which is subtended an angle t from the inertial axis). The primary body has (nondimensional) mass $1-\mu$; likewise, the secondary body has mass μ. The distance between the bodies is always 1. 4

2.3 The forbidden realm (grey) and the zero-velocity curves (its boundary) for the particle P with a given Jacobi constant C_J. Case 3 is the first instance where the particle P has full access to the entire space. The forbidden realm completely disappears in case 5. 6

2.4 An example trajectory in the PCR3BP with $\mu \ll 1$. Far away from the secondary m_2, the particle P (nearly) experiences a Keplerian trajectory with orbital elements (a, e, ν, ω) which relate to the Delaunay variables (L, G, l, g). The orbit is subject to change when P approaches m_2 and then stays constant again until the next close approach. This trajectory is shown *exterior* to m_2; however, a trajectory could also be shown *interior* to m_2. In this case, the close approach would occur at apoapse. The positioning of the bodies is drawn to scale with $\mu = 10^{-7}$. 8

2.5 Contours of the Tisserand parameter. The contour $C_J = 3$ is the one that includes the point $(a, e) = (1, 0)$, which corresponds to the secondary. Contours with $C_J > 3$ are restricted to either the interior or exterior of m_2 whereas $C_J \leqslant 3$ contours have full access everywhere. Ignoring transit trajectories between realms, this behavior agrees with Figure 2.3. 9

2.6 Diagram of the unstable manifolds $W^u(L_1)$ and $W^u(L_2)$ until their first apoapse and periapse, respectively. These events occur when the trajectory grazes the forbidden realm, corresponding to the Poincaré section $\{(x, y, \dot{x}, \dot{y}) \in \mathbb{R}^4 \mid \dot{r} = 0\}$, where $\dot{r}$ is given by (A.1). 10

2.7 Comparison of the (ω, a) phase space between the Keplerian map (**left**) and the true differential equations (**right**), which depict the evolution of 2BP-like trajectories through successive secondary encounters. This figure is adapted with permission from Ross and Scheeres [15]. 14

2.8 Comparison of the Keplerian map's phase space using the kick functions f (2.17) and $\tilde{f}$ (2.26) iterated $N = 2500$ times with 100 initial conditions. Here, $\mu = 10^{-6}$, $C_J = 3$, and $\bar{a} = -1/2\bar{K} = 0.75$ (interior motion). 16

3.1 A rotational invariant circle on the cylinder $\mathcal{C} = S^1 \times \mathbb{R}$. In terms of the Keplerian map, each RIC forms a continuous function $K = K(\omega)$, or equivalently $a = a(\omega)$, dividing the phase space into two distinct regions. Adapted with permission from Ross and Scheeres [15]. 17

3.2 Several periodic (magenta) and quasiperiodic (red, blue) trajectories shown over a small portion of phase space. (This behavior indeed extends across the cylinder.) The periodic trajectories comprise elliptic fixed points and, in order of appearance from top to bottom, are 20, 57, and 37-cycles. Respectively, these periodic orbits are of order 6, 20, and 13. They are surrounded by a family of librational circles (outlined in blue). The corresponding hyperbolic points are not shown. Bounding each family of librational circles is a family of rotational circles (outlined in red), or RICs. Note that each region bounded by RICs is isolated from the others. . . . 19

3.3 An identified RIC in the (ω, a) phase space. 20

3.4 **Left:** A cantorus. Each librational circle lies on a smooth curve which, when viewed all together, appear to fill out a graph, but they do not. **Right:** Similar, but chaotic. The regions have a thickness and becomes especially fuzzy near each separatrix. In cases where orbits are sparse or librations are stretched exceptionally thin, the cantorus is generally more difficult to rule out as an RIC. 21

3.5 **Left:** Librational circle under iterates of the map. **Right:** The same librational circle, but now treated as the function $a = a(\omega)$. 21

3.6 A quasiperiodic trajectory represented as the outer points of a star (shown to guide the eye) that returns close to its initial condition after five iterates. The initial condition is marked as blue and its return after performing an excursion is shown in red. Multiple excursions lead to regions that become filled with iterates separated by gaps. These gaps continue to narrow; for a large amount of excursions, the regions become indiscernible from one another as they densely pack together. This star evolution can be viewed as a trajectory *on* the cylinder (librational circle) and iterates of the angle *around* the cylinder (RIC). Note that when viewed on the cylinder, iterates tend to overlap themselves *before* the regions encounter each other for the first time (i.e. the initially large gap "closes"). 23

3.7 Defining the angle θ_n made between the vectors pointing to the next two neighboring points, x_{n+1} and x_{n+2}, from the current point x_n for arbitrary data in the (x, y) plane. The question to address is whether this data set lies on some differentiable curve (shown dashed) or not. 24

3.8 Growth of the distance from the primary during close approach for which energy kicks cease to provide meaningful transit. 26

3.9 **Left:** The first RIC in the interior Keplerian map with $\mu = 3.5 \times 10^{-5}$ and $C_J = 3$ (corresponding to the 7:4 resonance of Figure 3.8), which forms a continuous curve around the cylinder. **Middle:** The trajectory in the rotating frame. Note that because the RIC is a continuous curve, this is actually a densely filled annulus (which is the projection of the McGehee torus into configuration space). The chaotic zone r_{RIC} is the distance between this invariant surface's (average) outer boundary and the secondary. **Right:** The trajectory in the inertial frame; the elapsed time at the current iteration, required to transform into the inertial frame, is given by (2.22). The particle falls into a wobbling, frozen-like orbit due to the RIC's quasiperiodicity. 27

3.10 Evolution of RIC families above the 2:1 resonance as μ increases from 1.23×10^{-4} (top left) to 2.15×10^{-4} (bottom right). In this progression, the families become thinner and are pushed upwards, away from the hyperbolic fixed point located around $(\omega, a) = (\pi, (1/2)^{2/3})$. This behavior is generic for other $s : r$ resonances. . 28

3.11 Comparison of the RIC radius to other chaotic zone estimates. 29

4.1 Dimensionalization of one 3BP system in terms of the other. In this configuration, the particle's motion is interior to the departure system (labelled a distance 1 from the primary) and, similarly, exterior to the capture system (A). Note that the capture system is still a unit distance away from the primary in its *own* system (the other body being $1/A$). 32

4.2 Tisserand curves from two 3BP systems with a chosen Jacobi constant C_J and distance A intersect at a switching orbit. The switching orbit is closely surrounded by other potential switching orbits for slightly different Jacobi constants, forming a switching region. The switching orbit provides the means for the particle to switch being dominated by one 3BP system to the other. Here, the switching orbit is parameterized by $A = 2$ and $C_J = 3$. 33

4.3 The switching orbit lies in between the departure ($a \sim 1$) and capture ($a \sim A$) orbits. Its Tisserand parameter should be chosen such that it has close approaches to *both* systems. Not enough energy (too large of a Jacobi constant) pulls the switching orbit away from the bodies; too much energy (too low of a Jacobi constant) pushes the switching orbit too close to the bodies since it intersects their trajectories. 35

4.4 Improvement of the lower bounds for the Jacobi constant so that the reference orbits are nested between the bodies and the switching orbit for $\lambda = 0.5$. The green regions have no intersections between any orbits (to zeroth order in μ), so they serve as a good place to select a Jacobi constant for a given body with semimajor axis $a = A$. The grey regions can be selected, but the choice will likely not be as good because orbits will be intersecting each other to varying degrees of badness. The red region cannot be selected because it violates the constraint $0 < e < 1$. 37

4.5 The reference orbits (dashed) lie in between the departure/switching and capture/switching orbits. None of the curves intersect each other which means this Jacobi constant is admissible by Figure 4.4 (here $A = 1.5$, $C_J = 3$, and $\lambda = 0.5$). The switching orbit provides a means to exit one system while entering into the other; each reference orbit typically gets squeezed between the switching orbit and the perturbing body. 38

4.6 An example of an unpowered transfer trajectory with $C_J = 3$ from Earth to Venus. Every 50th orbit is drawn. The blue trajectories represents the particle in the Sun-Earth system, and the orange trajectories for the Sun-Venus system. 43

4.7 Continuation of the example trajectory shown in Figure 4.6. **Top:** Iterates of the initial conditions (circled in blue) in both Sun-Earth and Sun-Venus systems. The transfer is understood to occur in forward time (actually beginning at Earth and arriving at Venus), so the (forward) map $\mathbf{F}$ is used to traverse downwards in a and the inverse map $\mathbf{F}^{-1}$ upwards in a in each system. The motion in the Sun-Earth system is interior; the motion in the Sun-Venus system is exterior. Note that the two systems are plotted together on the same ω axis, but the two planets phase differently. Hence, one needs only check for proximity in K near the switching orbit. (Even if the trajectories don't align exactly in the switching region, continuity dictates that there exist trajectories that do.) **Left:** Evolution of the semimajor axis as viewed from the initial condition starting in the Earth's L_1 manifold orbit. This transfer, which is not optimized, takes 1391 years in total. **Right:** The particle moves along the energy surface provided by the Tisserand parameter. 44

List of Tables

2.1 Fits for the orbital elements (a, e) of the unstable manifolds $W^u(L_1)$ and $W^u(L_2)$ at their first apoapse/periapse. By time-reversal symmetry, these fits also describe the stable manifolds. 11

3.1 Chosen parameters for detecting RICs. 27

4.1 Summary of the parameters used to define the manifold, reference, and switching orbits for the Sun-Earth and Sun-Venus systems. These two systems are expressed in their *own* units; however, the Sun-Venus* system is expressed in units relative to the Sun-Earth system. The unstable and stable manifolds do not follow the energy surface induced by $C_J = 3$; instead, they have eccentricities $e_{W^u(L_1)} = 2.962 \times 10^{-2}$ and $e_{W^s(L_2)} = 2.837 \times 10^{-2}$. These orbits respectively correspond to Tisserand parameters $C_{JW^u(L_1)} = 3.00027231$ and $C_{JW^s(L_2)} = 3.00027033$. 42

4.2 A sample set of initial conditions in the Sun-Earth and Sun-Venus systems that resulted in transfer between the two bodies. 43

List of Abbreviations

2BP	2-Body Problem
FLI	Fast Lyapunov Indicator
FTLE	Finite Time Lyapunov Exponent
PCCR4BP	Planar Concentric Circular 4-Body Problem
PCR3BP	Planar Circular Restricted 3-Body Problem
RIC	Rotational Invariant Circle
SOI	Sphere of Influence
TOF	Time of Flight

Chapter 1

Introduction

In recent decades, much work has been done on the three-body problem, especially related to low energy transfers. Such trajectories were first discovered in the late 1960s going back to Conley and McGehee and then in the early 1990s with Belbruno and Miller in their low energy ballistic capture by the moon. Much of this work investigates how low energy ballistic capture is mediated by invariant manifold structures, which are related to the Lagrange points that govern transit to the planetary realm – the realm around the secondary – from the interior and exterior realms. But there is still work to be done looking at the rich dynamics in just the exterior and just the interior realms. Developed in 2007, the Keplerian map is an excellent reduced order model for studying this and allows one to co-opt the rich literature on symplectic maps such as in Meiss [12] and references therein.

Parts of the 4D phase space, like the McGehee tori that exist in the interior and exterior regions bounding low energy motion, can be understood in terms of dynamics admitted by the map in the form of rotational invariant circles. Such an investigation is relevant as it adds to the literature of chaotic zone characterizations about the secondary and, further, provides an indication if a transfer between given bodies in a patched 4-body setting is possible. This transfer is directly effected by repeated gravity assists on each secondary without the use of any external energy sources such as propulsion systems, which has relevance to dynamical astronomy (e.g., ejecta from one body transferring to another) and mission design (e.g., a multi-moon orbiter wanting to save fuel). Ultimately, the Keplerian map is a tool that can be used to seek desirable regions of phase space for initial conditions resulting in multibody transfer within the continuous problem.

The structure of this thesis is as follows. Chapter 2 introduces the planar circular restricted 3-body problem (PCR3BP) in continuous time. Simplifying assumptions are then made to approximate the dynamics in discrete time as a 2D area-preserving (symplectic) twist map, referred to as the Keplerian map. Chapter 3 investigates the dynamics of this map to provide a characterization of the chaotic zone surrounding the secondary body by means of rotational invariant circles. Chapter 4 then demonstrates the method of seeking transfers by providing an example trajectory between Earth and Venus. Chapter 5 summarizes the current findings.

Chapter 2

Dynamical models

Within a region of the solar system dominated by only three celestial bodies, the motion of a particle P is well-described by the restricted 4-body problem. A typical configuration of the problem is shown by Figure 2.1a, in which two of the bodies (planets or moons) orbit a common central body (the sun or a planet) in a 2-body fashion. Under simplification, the orbits are circularized and the central body held fixed as in Figure 2.1b; this is the planar concentric circular restricted 4-body problem (PCCR4BP). Despite this model *not* satisfying Newton's laws of motion, it still provides insightful dynamics useful for exploring solutions within the true ephemeris. Particularly, one can leverage the rich features of three-body dynamics by considering the particle P patched between the $m_1 - m_2 - P$ and $m_1 - m_3 - P$ systems, each of which resembles the planar circular restricted 3-body problem (PCR3BP).

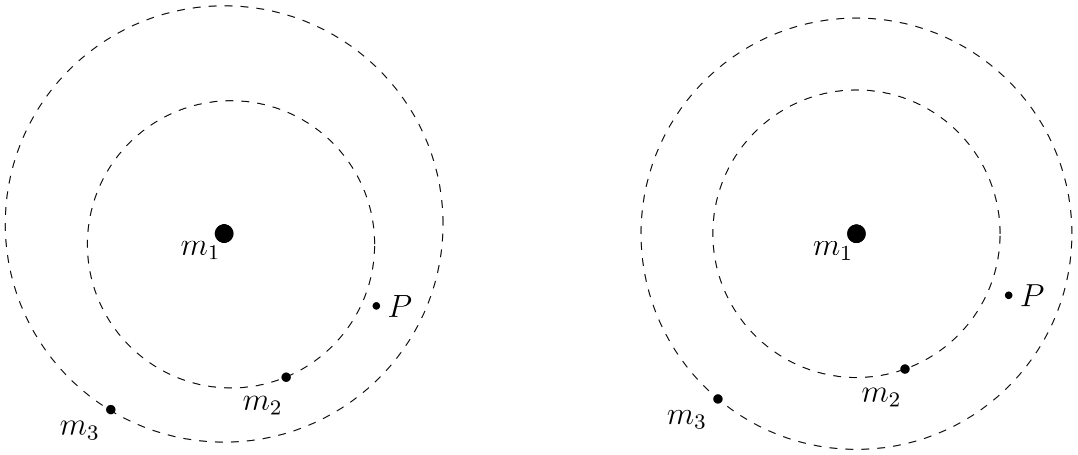

(a) m_2, m_3 orbiting m_1 as in the solar system (b) m_2, m_3 orbiting m_1 in concentric circles

Figure 2.1: Approximating dynamically accurate trajectories as circular orbits (PCCR4BP).

2.1 Continuous dynamics

The planar circular restricted 3-body problem (PCR3BP) is formulated in a nondimensional coordinate system rotating with unit angular velocity (relative to the inertial frame) such that the two bodies of masses m_1 and m_2, with $m_2 \leqslant m_1$, appear stationary. Their masses and distances from their barycenter (the origin) are given in terms of the mass parameter μ defined

$$\mu := \frac{m_2}{m_1 + m_2}. \tag{2.1}$$

The mass parameter always satisfies $\mu \leqslant 0.5$, though physically relevant mass parameters found throughout the solar system are often much smaller (with the exception of special cases like the Pluto-Charon pair). Newton's gravitational constant $G = 1$ is also dimensionless in this system of units. Figure 2.2 shows the PCR3BP in the rotating frame with the particle P located at the (spatial) coordinates (x, y) a distance r from the origin. The distances r_1 and r_2 from the primary and secondary, respectively, to P follow similarly.

$$\begin{aligned} r_1^2 &= (x + \mu)^2 + y^2 \\ r_2^2 &= (x + \mu - 1)^2 + y^2 \end{aligned} \tag{2.2}$$

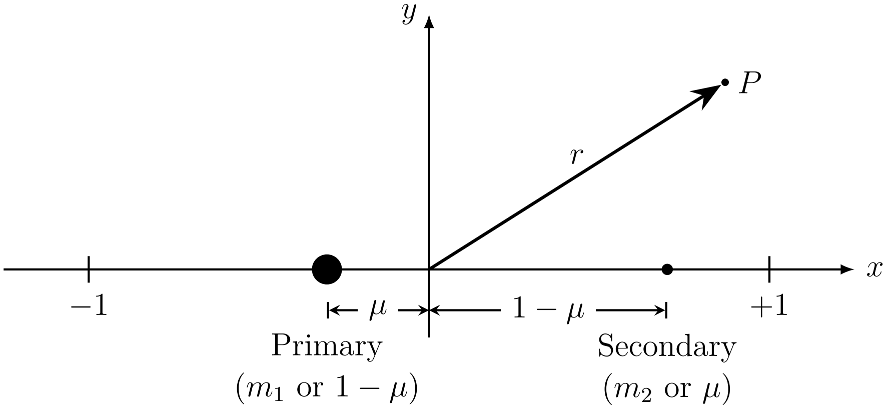

Figure 2.2: The PCR3BP in the rotating frame (which is subtended an angle t from the inertial axis). The primary body has (nondimensional) mass $1 - \mu$; likewise, the secondary body has mass μ. The distance between the bodies is always 1.

2.1.1 The Hamiltonian

In the rotating frame, the PCR3BP admits a set of autonomous differential equations providing the dynamics of the particle P. This motion is often described in *velocity coordinates* $(x, y, \dot{x}, \dot{y}) \in \mathbb{R}^4$ or *momentum coordinates* $(x, y, p_x, p_y) \in \mathbb{R}^4$. In the latter case, Hamilton's canonical equations provide a source for the particle's motion with the Hamiltonian function $H : \mathbb{R}^4 \to \mathbb{R}$ written

$$H = \underbrace{\frac{1}{2}\left((p_x + y)^2 + (p_y - x)^2\right)}_{\text{kinetic energy in the rotating frame}} + \underbrace{\left(-\frac{1}{2}(x^2 + y^2) - \frac{1-\mu}{r_1} - \frac{\mu}{r_2} - \frac{1}{2}\mu(1-\mu)\right)}_{\text{effective potential energy}}. \tag{2.3}$$

The velocities $(\dot{x}, \dot{y})$ and momenta (p_x, p_y) are related via their Legendre transform [5].

$$\begin{aligned} p_x &= \dot{x} - y \\ p_y &= \dot{y} + x \end{aligned} \tag{2.4}$$

By Hamilton's equations, the momenta have the dynamics $\dot{p}_x = -H_x$ and $\dot{p}_y = -H_y$, or

$$\begin{aligned} \dot{p}_x &= +p_y - \frac{(1-\mu)(x+\mu)}{((x+\mu)^2 + y^2)^{3/2}} - \frac{\mu(x+\mu-1)}{((x+\mu-1)^2 + y^2)^{3/2}} \\ \dot{p}_y &= -p_x - \frac{(1-\mu)y}{((x+\mu)^2 + y^2)^{3/2}} - \frac{\mu y}{((x+\mu-1)^2 + y^2)^{3/2}}. \end{aligned} \tag{2.5}$$

These four relations completely describe the particle's motion in the PCR3BP via momentum coordinates. The corresponding dynamics in terms of velocity coordinates can be obtained by differentiation of (2.4) and combining it with (2.5).

Although similar in expression, several notable qualities leave these two sets of coordinates significantly different from one another. In particular for this work, velocity coordinates are convenient for numerical integration/coordinate transformations, whereas momentum coordinates are useful for theoretical developments. Namely that $(p_x^2 + p_y^2)/2$ is the inertial kinetic energy and the dynamics in the (x, y, p_x, p_y) phase space are *symplectic*, or area-preserving [2, 5].

2.1.2 Jacobi's constant & Lagrange points

The Hamiltonian (2.3) is explicitly independent of time and thus a constant of motion [5, 13, 17]. From this, the *Jacobi constant* is taken to be

$$C_J := -2H \tag{2.6}$$

and thus relates to the energy. In particular, considering where the (rotating frame's) kinetic energy vanishes gives rise to the *zero-velocity curves*, which implicitly show the possible regions of motion for a given Jacobi constant. A well-known result is that these zero-velocity curves are split into five cases — notably, the curves completely disappear for $C_J \leqslant 3$.

These zero-velocity curves bifurcate at the five *Lagrange points*, which are the PCR3BP's equilibria [5]. This set comprises the three collinear points (L_1, L_2, and L_3) and two triangular points (L_4 and L_5). The ones of particular interest here are nearest to the secondary, L_1 and L_2, corresponding to the locations of the zero-velocity curve bifurcations occurring at $C_J = C_1$ and $C_J = C_2$ in Figure 2.3. These points are given special attention since they govern minimal-energy transit trajectories between realms. Their locations follow from the (unique) real solutions to a set of quintic polynomials [5, 17].

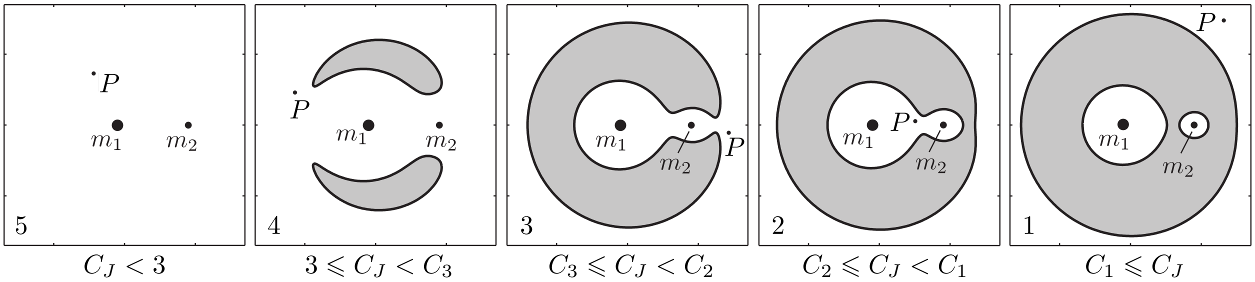

Figure 2.3: The forbidden realm (grey) and the zero-velocity curves (its boundary) for the particle P with a given Jacobi constant C_J. Case 3 is the first instance where the particle P has full access to the entire space. The forbidden realm completely disappears in case 5.

2.2 Small-body approximation

2.2.1 Decomposing the Hamiltonian

Under the assumption $\mu \ll 1$, where the PCR3BP is considered a perturbation of the 2-body problem (2BP), Ross and Scheeres [15] write the Hamiltonian (2.3) expressed as

$$H = \underbrace{\left(\frac{p_x^2 + p_y^2}{2} - \frac{1}{r}\right)}_{K} - \underbrace{\sqrt{a(1-e^2)}}_{G} + \mu \underbrace{\left(\frac{\cos\theta}{r^2} - \frac{1}{\sqrt{r^2 - 2r\cos\theta + 1}} + \frac{1}{r}\right)}_{R} + \mathcal{O}(\mu^2), \quad (2.7)$$

where (p_x, p_y) are the canonical momenta and (r, θ), shown in Figure 2.4, follow from the 2BP. Particularly when $\mu \ll 1$, the distances r and r_1 are equal up to $\mathcal{O}(\mu)$ and θ is the argument of latitude in the rotating frame.

$$r = \frac{a(1-e^2)}{1 + e\cos\nu}, \qquad \theta = \bar{\omega} + \nu \quad (2.8)$$

Here, the semimajor axis a, eccentricity e, and true anomaly ν of the particle's orbit about the primary are in the usual sense of the 2BP; however, $\bar{\omega}$ is the argument of periapse in the *rotating* frame. Its relation to the usual argument of periapse ω is given by inspection of Figure 2.4. Further, G and K are the particle's 2BP angular momentum and vis viva integral in a system with a central mass 1. This integral, called the *Keplerian energy*, consequently relates to the semimajor axis as [1, 13]

$$K := -\frac{1}{2a}. \quad (2.9)$$

Delaunay variables

The Hamiltonian (2.7) is in a desirable form since a transformation into Delaunay variables $(L, G, l, \bar{g}) \in \mathbb{R}^4$, a set of action-angle variables, is proper. The *angles* l and $\bar{g}$ are conjugate to the *actions* L and G, respectively; in particular, they abide by Hamilton's canonical equations.

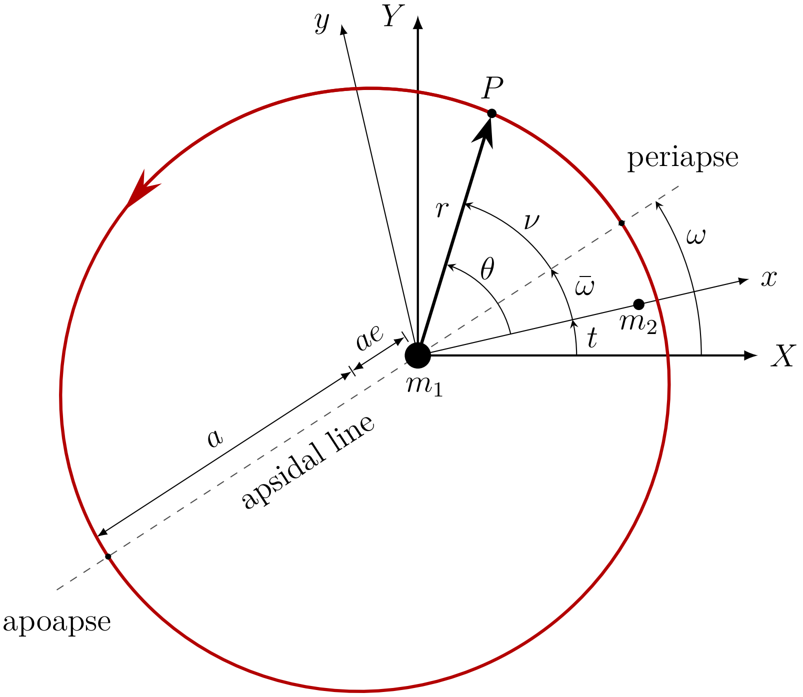

Figure 2.4: An example trajectory in the PCR3BP with $\mu \ll 1$. Far away from the secondary m_2, the particle P (nearly) experiences a Keplerian trajectory with orbital elements (a, e, ν, ω) which relate to the Delaunay variables (L, G, l, g). The orbit is subject to change when P approaches m_2 and then stays constant again until the next close approach. This trajectory is shown *exterior* to m_2; however, a trajectory could also be shown *interior* to m_2. In this case, the close approach would occur at apoapse. The positioning of the bodies is drawn to scale with $\mu = 10^{-7}$.

In terms of orbital elements, the angles l and $\bar{g}$ are the mean anomaly and the rotating frame's argument of periapse, respectively (i.e., $l \equiv M$ and $\bar{g} \equiv \bar{\omega}$) [17]. The actions are

$$\begin{aligned} L &:= \sqrt{a} \\ G &:= L\sqrt{1-e^2}, \end{aligned} \tag{2.10}$$

where appears the angular momentum G. Consequently, the Hamiltonian (2.7) becomes

$$H = -\frac{1}{2L^2} - G + \mu R + \mathcal{O}(\mu^2). \tag{2.11}$$

The disturbing function in these variables takes the form $R = R(L, G, l, \bar{g})$.

The transformation into Delaunay variables from velocity coordinates $(x, y, \dot{x}, \dot{y})$ is also useful. From an integration of the differential equations, (2.10) permits a direct (i.e., time-independent) realization of the osculating elements (a, e) determining the orbit's geometry; its orientation in the plane is given by $g = \bar{g} + t$, which is the argument of periapse in the inertial frame. The full transformation $(x, y, \dot{x}, \dot{y}) \mapsto (L, G, l, \bar{g})$ is provided in Appendix A.

2.2.2 Tisserand's parameter & manifolds of the Lagrange points

Inserting the Hamiltonian (2.11) into (2.6), the Jacobi constant expressed in terms of orbital elements is

$$C_J = \frac{1}{a} + 2\sqrt{a(1-e^2)} + \mathcal{O}(\mu). \tag{2.12}$$

The terms up to leading order are called the *Tisserand parameter* which approximates the motion's true Jacobi constant in the PCR3BP [13]. Thus, the Tisserand parameter is nearly

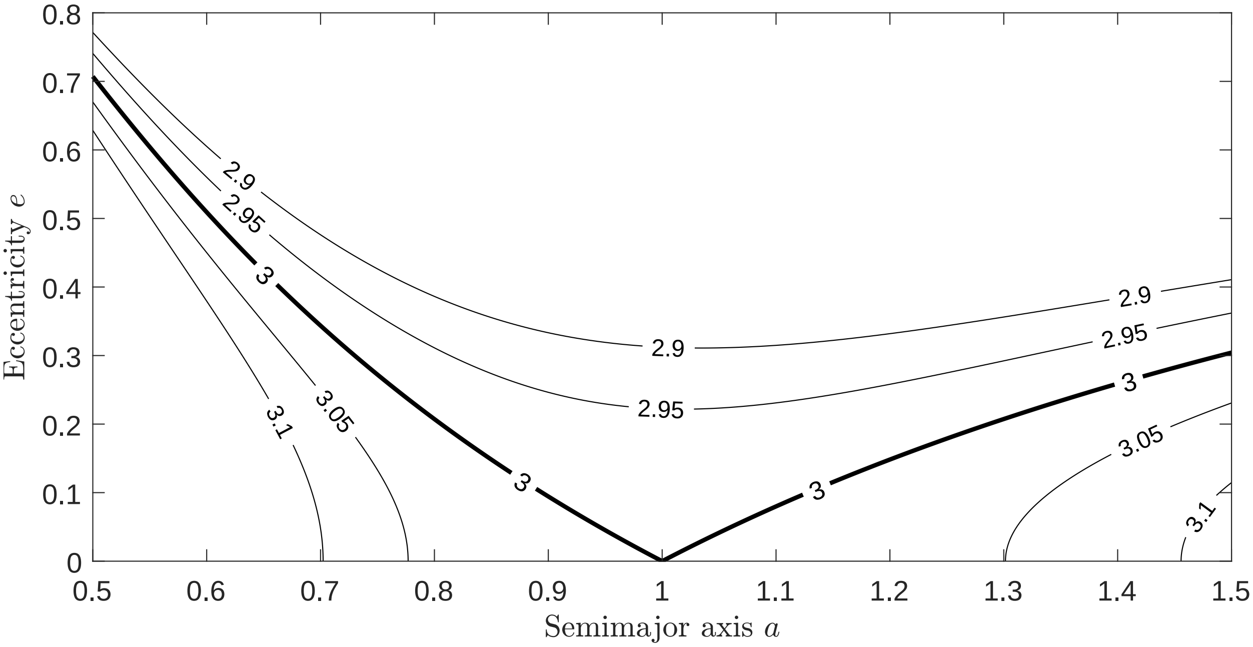

Figure 2.5: Contours of the Tisserand parameter. The contour $C_J = 3$ is the one that includes the point $(a, e) = (1, 0)$, which corresponds to the secondary. Contours with $C_J > 3$ are restricted to either the interior or exterior of m_2 whereas $C_J \leqslant 3$ contours have full access everywhere. Ignoring transit trajectories between realms, this behavior agrees with Figure 2.3.

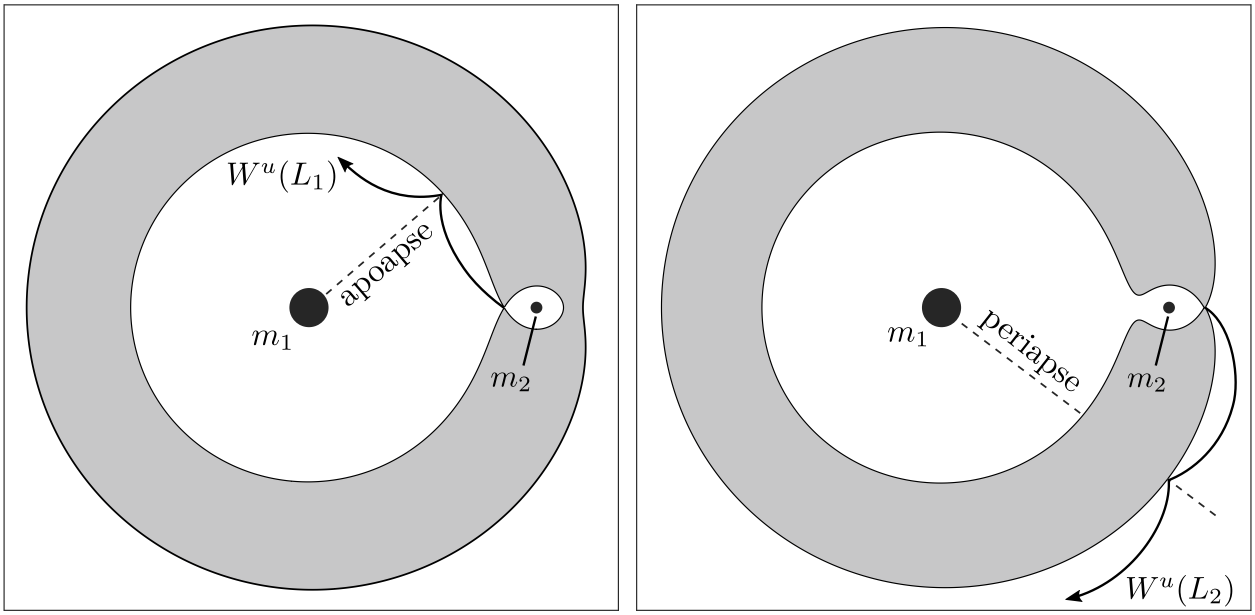

Figure 2.6: Diagram of the unstable manifolds $W^u(L_1)$ and $W^u(L_2)$ until their first apoapse and periapse, respectively. These events occur when the trajectory grazes the forbidden realm, corresponding to the Poincaré section $\{(x, y, \dot{x}, \dot{y}) \in \mathbb{R}^4 \mid \dot{r} = 0\}$, where $\dot{r}$ is given by (A.1).

constant for motion in systems with $\mu \ll 1$. In this case, the $\mathcal{O}(\mu)$ terms are dropped and the Tisserand parameter is identified with the Jacobi constant C_J to ease notation. This relation is especially useful for writing the eccentricity as $e = e(a; C_J)$ so that an orbit's geometry is specified by its semimajor axis and Tisserand parameter. Figure 2.5 shows the possible trajectories for a given Tisserand parameter.

With $\mu \ll 1$, the manifolds emanating from the Lagrange points can be characterized too in terms of semimajor axis a, eccentricity e, and argument of periapse (in the rotating frame) $\bar{\omega}$. These special 2BP trajectories serve as proxies for the capture/escape trajectories enclosed by the manifolds winding onto and off of the Lyapunov orbits [9]. To ensure sufficient distance from the secondary so that a 2BP trajectory is effectively established, the orbital elements are taken at apoapse when interior to m_2, and at periapse when exterior to m_2, as shown in Figure 2.6.

Accurate curve fits of these manifolds at their first apoapse/periapse can be found in the following manner. Let L_i with $i = 1, 2$ be the equilibrium point being considered at the coordinates $\mathbf{x}_{eq} = (x, y, \dot{x}, \dot{y})_{eq} = (L_i, 0, 0, 0)$ and

$$\bar{\mu} := \frac{\mu}{|L_i + \mu - 1|^3} + \frac{1-\mu}{|L_i + \mu|^3}. \tag{2.13}$$

Then the linearization about this point L_i provides dynamics with the unstable manifold's eigenvalue and corresponding eigenvector (where λ is used unambiguously) [5].

$$\lambda_{W^u(L_i)} = \sqrt{\frac{\bar{\mu} - 2 + \sqrt{9\bar{\mu}^2 - 8\bar{\mu}}}{2}}, \qquad \mathbf{v}_{W^u(L_i)} = \begin{bmatrix} 1 \\ \lambda(\lambda^2 - 2\bar{\mu} + 3)/(2 - 2\bar{\mu}) \\ \lambda \\ (\lambda^2 - 2\bar{\mu} - 1)/2 \end{bmatrix} \tag{2.14}$$

Now let $\phi : \mathbb{R} \times \mathbb{R}^4 \to \mathbb{R}^4$ be the family of flow maps generating the trajectory $\mathbf{x}(t)$ from the initial condition $\mathbf{x}_0$ such that $\mathbf{x}(t) = \phi(t, \mathbf{x}_0)$. The trajectory $\phi(t, \mathbf{x}_{eq} + \epsilon\hat{\mathbf{v}})$, where $|\epsilon| \ll 1$ is a small perturbation, shadows the unstable manifold for $t > 0$. In particular, choosing t large enough eventually results in the trajectory grazing the forbidden realm, revealing characteristics about the manifold's semimajor axis a and eccentricity e when $\mu \ll 1$ as shown in Figure 2.6.

Using the above procedure, the unstable (and stable) manifolds of L_1 and L_2 are found to be well approximated by fitting quadratic curves in the spaces $(\ln\mu, \ln e)$ and (e, a) for some constants $\alpha, \beta, \gamma, \delta, \varepsilon \in \mathbb{R}$.

$$e(\mu) = \alpha\mu^{\beta \ln\mu + \gamma}, \qquad a(\mu) = \delta e^2 + \varepsilon e + 1 \tag{2.15}$$

Table 2.1: Fits for the orbital elements (a, e) of the unstable manifolds $W^u(L_1)$ and $W^u(L_2)$ at their first apoapse/periapse. By time-reversal symmetry, these fits also describe the stable manifolds.

Manifold	α	β	γ	δ	ε
$W^u(L_1)$	1.6342	-1.0433×10^{-3}	0.3002	1.3275	-1.6004
$W^u(L_2)$	2.9066	1.2594×10^{-3}	0.3727	1.8096	1.5666

2.3 Discrete dynamics

2.3.1 The Keplerian map

Using the Hamiltonians (2.7) and (2.11) up to $\mathcal{O}(\mu)$, Ross and Scheeres [15] provide a discrete-time approximation, coined the *Keplerian map* $\mathbf{F} : \mathcal{C} \to \mathcal{C}$, where $\mathcal{C} = S^1 \times \mathbb{R}$ is the cylinder, of the particle's motion at its apses (either periapse or apoapse) with orbital elements (ω, a, e).

$$\begin{bmatrix} \omega_{n+1} \\ K_{n+1} \end{bmatrix} := \underbrace{\begin{bmatrix} \omega_n - 2\pi(-2K_{n+1})^{-3/2} \\ K_n + \mu f(\omega_n) \end{bmatrix}}_{\mathbf{F}(\omega_n, K_n)} \tag{2.16}$$

Historically, ω here refers to the argument of periapse *in the rotating frame* (i.e., $\bar{\omega}$, but the bar notation is dropped) and is not to be confused with the typical 2BP argument of periapse ω. The map has twist to the left (erroneously claimed to the right by previous references [3, 15]) and is posed in terms of the energy K (instead of the semimajor axis a) to ensure that the dynamics can be symplectic like the original differential equations in momentum coordinates. The eccentricity e is induced by the Tisserand parameter C_J so that every trajectory is bound to move along a single contour of Figure 2.5 via the *kick function* $f : S^1 \to \mathbb{R}$ written

$$\begin{aligned} f(\omega) := &-\frac{1}{\sqrt{a(1-e^2)}} \int_{S^1} \left(\frac{r^3}{(r^2 - 2r\cos(\omega - t(\nu) + \nu) + 1)^{3/2}} - 1 \right) \sin(\omega - t(\nu) + \nu)\, d\nu \\ &- \frac{1}{\sqrt{Q^2 + 2Q\cos(\omega + \tau) + 1}} + \frac{1}{\sqrt{Q^2 + 2Q\cos(\omega - \tau) + 1}} + \frac{2\sin\tau\sin\omega}{Q^2}. \end{aligned} \tag{2.17}$$

Here, $Q = a(1+e)$ and $\tau = \pi a^{3/2}$ are the apoapse distance and half-period, respectively, of the (**reference**) 2BP trajectory $r = r(\nu)$ with semimajor axis a and eccentricity e as given by (2.8). The kick function is integrated over S^1 representing one period of motion; numerically, its features are better resolved using the interval $(-\pi, \pi)$ if $a > 1$ (the *exterior/periapse kick function*) and $(0, 2\pi)$ if $a < 1$ (the *interior/apoapse kick function*). With these two cases in mind, the time $t = t(\nu)$ over which the orbit acts is compactly written

$$t(\nu) = a^{3/2} M(\nu) - \tau u(1 - a), \tag{2.18}$$

where M is the mean anomaly satisfying Kepler's equation and $u(\cdot)$ the unit step function. Further, the Keplerian map $\mathbf{F}$ admits an inverse so that backwards iteration is well-defined.

$$\begin{bmatrix} \omega_{n-1} \\ K_{n-1} \end{bmatrix} := \underbrace{\begin{bmatrix} \omega_n + 2\pi(-2K_n)^{-3/2} \\ K_n - \mu f(\omega_{n-1}) \end{bmatrix}}_{\mathbf{F}^{-1}(\omega_n, K_n)} \tag{2.19}$$

In both interior and exterior cases, the Keplerian map is denoted $\mathbf{F}$ since it is implied clearly which one is used for motion inside and outside of the secondary. This mapping $\mathbf{F}$ corresponds to a 2BP trajectory with orbital elements (ω_n, a_n, e_n) becoming $(\omega_{n+1}, a_{n+1}, e_{n+1})$ after a close approach with the secondary in forward time (similarly, $\mathbf{F}^{-1}$ in backwards time).

With an initial 2BP trajectory corresponding to the elements (ω_0, K_0), the Keplerian map generates a *trajectory* T in the (ω, K) phase space as

$$T^N_{(\omega_0, K_0)} := \left\{ \mathbf{F}^n(\omega_0, K_0) \in \mathcal{C} \mid n = 0, \ldots, N \text{ with } N \in \mathbb{Z} \right\}. \tag{2.20}$$

Here, $\mathbf{F}^n$ indicates function composition (i.e., for some $k \geqslant 1$, $\mathbf{F}^k = \mathbf{F} \circ \mathbf{F}^{k-1}$ and similarly $\mathbf{F}^{-k} = \mathbf{F}^{-1} \circ \mathbf{F}^{-k+1}$) with $\mathbf{F}^0$ the identity. Hence, $T^N_{(\omega_0, K_0)}$ is never empty. Note that the inverse map enables a trajectory to be "centered" on the coordinates (ω_0, K_0); it can be established as $T^{M,N}_{(\omega_0, K_0)} := T^M_{(\omega_0, K_0)} \cup T^N_{(\omega_0, K_0)}$ for some $M \leqslant 0 \leqslant N$. The bi-infinite trajectory centered on the coordinates (ω_0, K_0), if it exists, is called an *orbit* O [19] and is denoted

$$O_{(\omega_0, K_0)} := \lim_{N \to \infty} T^{-N,N}_{(\omega_0, K_0)}. \tag{2.21}$$

Let $\mathbb{T} := \{ T^N_{(\omega_0, K_0)} \mid (\omega_0, K_0) \in \mathcal{C}, N \in \mathbb{Z} \}$ be the set of all trajectories and, similarly, $\mathbb{O}$ the set of all orbits. The elapsed time (or time of flight) $\Delta t : \mathbb{T} \to \mathbb{R}$ over a trajectory is

$$\Delta t = 2\pi \sum_n a_n^{3/2}. \tag{2.22}$$

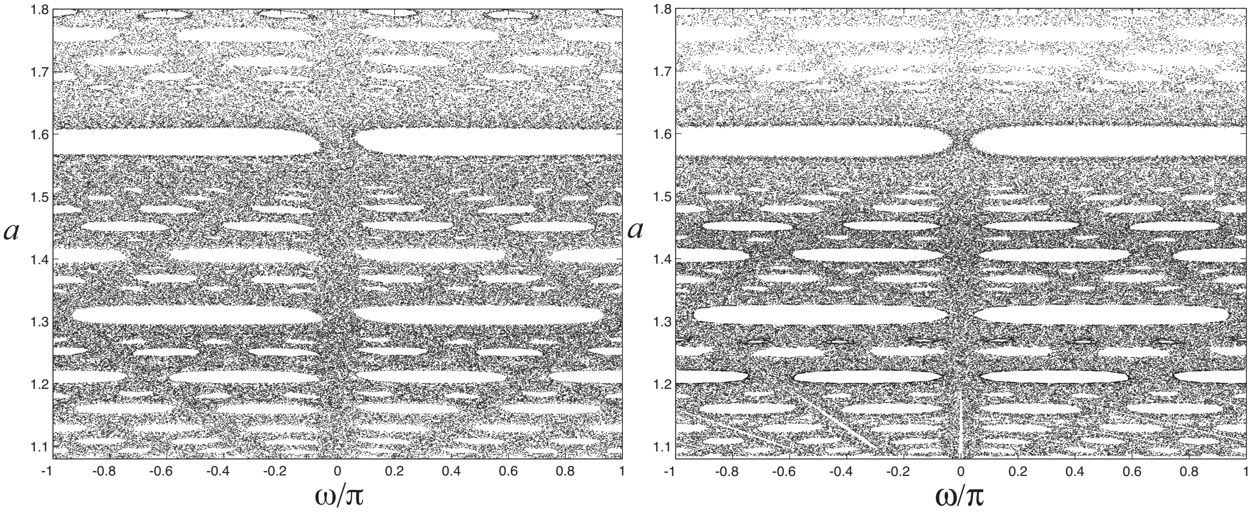

Figure 2.7: Comparison of the (ω, a) phase space between the Keplerian map (**left**) and the true differential equations (**right**), which depict the evolution of 2BP-like trajectories through successive secondary encounters. This figure is adapted with permission from Ross and Scheeres [15].

Local approximation about a reference trajectory

A necessary and sufficient condition for the Keplerian map to be symplectic is that the kick function f be independent of the energy K [15]. This requirement is fulfilled by choosing a particular energy $K = \bar{K}$, where $\bar{K}$ is constant, furnishing a *reference trajectory* described by all parameters of f (i.e., a, e, Q, and τ all must be constant). Thus, the reference orbit's orientation ω is its only degree of freedom.

Nearby orbits with energies similar to $\bar{K}$ experience similar dynamics through the Keplerian map — that is, the reference trajectory "tangentially approximates" the orbits surrounding it. Let $\{K_1 < K < K_2 < 0 \mid C_J = \text{const.}\}$ be the set of trajectories with a fixed Tisserand parameter (i.e. orbits following a single contour of Figure 2.5) between the energies K_1 and K_2. Then one way to pick the reference energy may be

$$\bar{K} := \kappa K_1 + (1 - \kappa) K_2, \tag{2.23}$$

where $\kappa \in [0, 1]$ is to be chosen — a popular choice being $\kappa = 0.5$. Equivalently, one can also write the reference energy in terms of the semimajor axes a_1 and a_2, respectively,

$$\bar{a} := \lambda a_1 + (1-\lambda) a_2 \tag{2.24}$$

The mixing parameters κ and λ differ by the relation

$$\frac{1}{\lambda} - \frac{\gamma}{\kappa} = 1 - \gamma, \tag{2.25}$$

where $\gamma = K_2/K_1 = a_1/a_2$. Despite this simplification seemingly leading to inaccuracies, numerical evidence shows that a reference trajectory is desirable as it results in a phase space structure resembling the true dynamics while also enabling high computational efficiency [15].

A topologically equivalent kick function

An analytic approximation of the kick function f is readily available and useful. The integrand of (2.17) can be evaluated at $\nu = \pi u(1-a)$, which produces the curve

$$\begin{aligned}\tilde{f}(\omega) := &-\frac{\sigma}{\sqrt{a(1-e^2)}}\left(\frac{\mathcal{Q}^3}{(\mathcal{Q}^2 - 2\sigma\mathcal{Q}\cos\omega + 1)^{3/2}} - 1\right)\sin\omega \\ &- \frac{1}{\sqrt{Q^2 + 2Q\cos(\omega+\tau) + 1}} + \frac{1}{\sqrt{Q^2 + 2Q\cos(\omega-\tau) + 1}} + \frac{2\sin\tau\sin\omega}{Q^2}\end{aligned} \tag{2.26}$$

where $\mathcal{Q} = a(1+\sigma e)$ and $\sigma = \operatorname{sgn}(1-a)$. Having similar magnitude and other desirable properties of the kick function, this expression may be inserted into the Keplerian map while qualitatively preserving the phase space as seen in Figure 2.8.

Notably, $\tilde{f}$ (2.26) requires less setup and computational resources, and is thus significantly faster in its evaluation, than f (2.17). Moreover, the preservation of phase space relaxes concerns of trajectories being artificially created due to numerical error since such perturbations to f are much smaller than replacing f altogether with $\tilde{f}$. These facts are advantageous when merely exploring the phase space to seek the existence of particular orbits, which often can require a large amount of iterations. Once existence is established, however, the kick function f should be used during the actual evaluation.

Historically, the second line of the kick function f (and therefore $\tilde{f}$) is ignored due to its small effects in the exterior region. In the interior region, however, new bumps are introduced (see Figure 2.8 near $\omega/\pi = 0.35$ and $\omega/\pi = 1.65$), but their effects are still minimized by the dominating double spike. Going forward, only the first line in f is used. Still, numerical evidence indicates that results obtained this way are preserved under the full kick function.

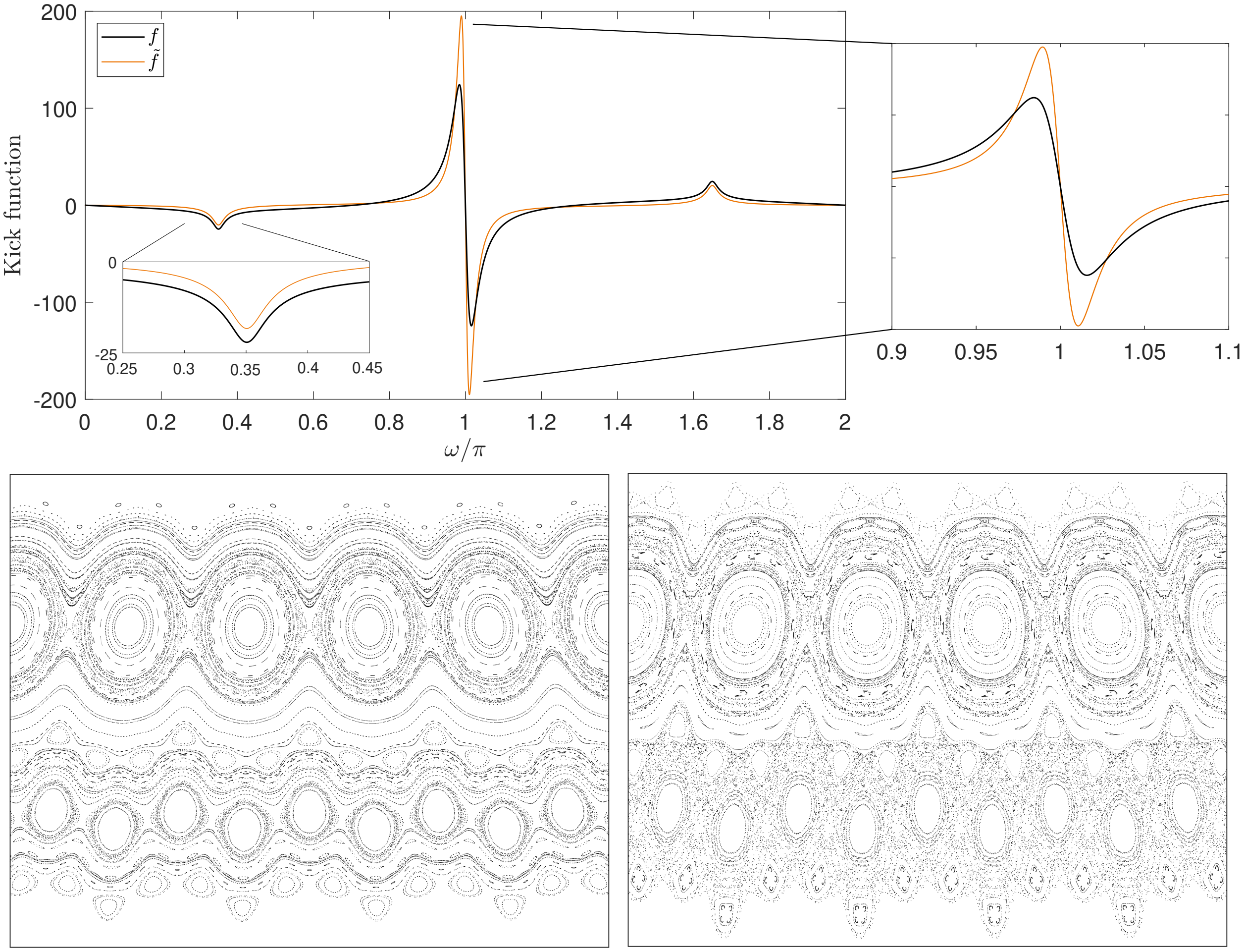

(a) (ω, K) phase space using f

(b) (ω, K) phase space using $\tilde{f}$

Figure 2.8: Comparison of the Keplerian map's phase space using the kick functions f (2.17) and $\tilde{f}$ (2.26) iterated $N = 2500$ times with 100 initial conditions. Here, $\mu = 10^{-6}$, $C_J = 3$, and $\bar{a} = -1/2\bar{K} = 0.75$ (interior motion).

Chapter 3

A boundary of chaotic transport

The Keplerian map effects change in the particle's 2BP trajectory via the kick function which models energy gained/lost during a close approach to the secondary. Like all models, however, the map has its limitations. In particular, trajectories must be bounded and within the chaotic zone. Previous characterizations of chaotic zones have been studied by Wisdom, Malhotra, and others in which the particle starts on circular or nearly parabolic orbits [6, 7, 10, 14, 20]. These scenarios do not fit well with the Keplerian map's capabilities, so a new measure of the chaotic zone is needed. The characterization of such a boundary is given by a *rotational invariant circle* (RIC), specifically the RIC closest to the secondary.

RICs are quasiperiodic orbits that serve as barriers to transport in phase space. That is,

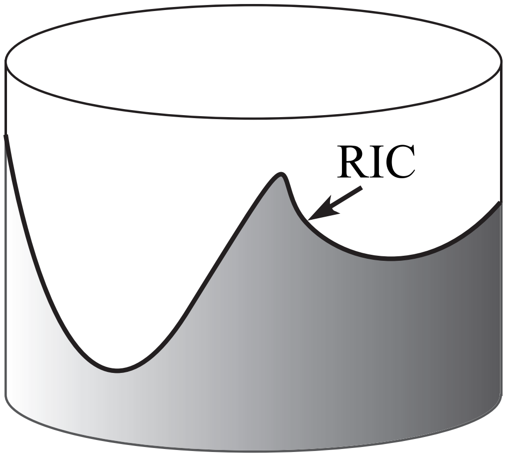

Figure 3.1: A rotational invariant circle on the cylinder $\mathcal{C} = S^1 \times \mathbb{R}$. In terms of the Keplerian map, each RIC forms a continuous function $K = K(\omega)$, or equivalently $a = a(\omega)$, dividing the phase space into two distinct regions. Adapted with permission from Ross and Scheeres [15].

the orbit $O \in \mathbb{O}$ forms an RIC, a continuous curve encircling the cylinder, if $O = \mathbf{F}(O)$ so that $a = a(\omega)$ [12, 15]. Paired with continuity over initial conditions, RICs naturally define a boundary indicating the extent to which a particle can be transported. Thus, determining the Keplerian map's bounding RICs is a fundamental research objective.

3.1 Classifying trajectories

Symplectic twist maps admit three classes of trajectories: **periodic**, **quasiperiodic**, and **chaotic** [12]. A periodic orbit with period n, called an n-cycle, is one that repeats itself every n iterates. Each iterate in the orbit, therefore, is a fixed point of the map $\mathbf{F}^n$ [16]. The Keplerian map contains both hyperbolic and elliptic fixed points [15]. Ultimately, the hyperbolic points are what govern transit while each elliptic (neutrally stable) point is surrounded by a resonance zone. These two kinds of fixed points alternate along a given $s : r$ band of resonances, where the particle completes $s \in \mathbb{N}$ orbits for every $r \in \mathbb{N}$ complete orbits of the secondary [15]. The band is located at $a = (r/s)^{2/3}$ and its *order* is $|s - r|$.

A quasiperiodic orbit is one that is nearly periodic; it can perform an excursion and almost come back to where it started. More precisely, it returns arbitrarily close to its initial condition. Quasiperiodicity on the cylinder comes in two flavors: **librational** and **rotational** motion [12]. Both kind of orbits form closed curves homeomorphic to a circle, but librational circles enclose themselves *on* the cylinder whereas rotational circles enclose themselves *around* the cylinder (see Figure 3.2).

Chaotic trajectories are (loosely) characterized by having sensitive dependence on initial conditions [12, 16]. Typically a chaotic trajectory will traverse the phase space (by means of lobe dynamics) over many iterations while departing from the structures by which they may have started.

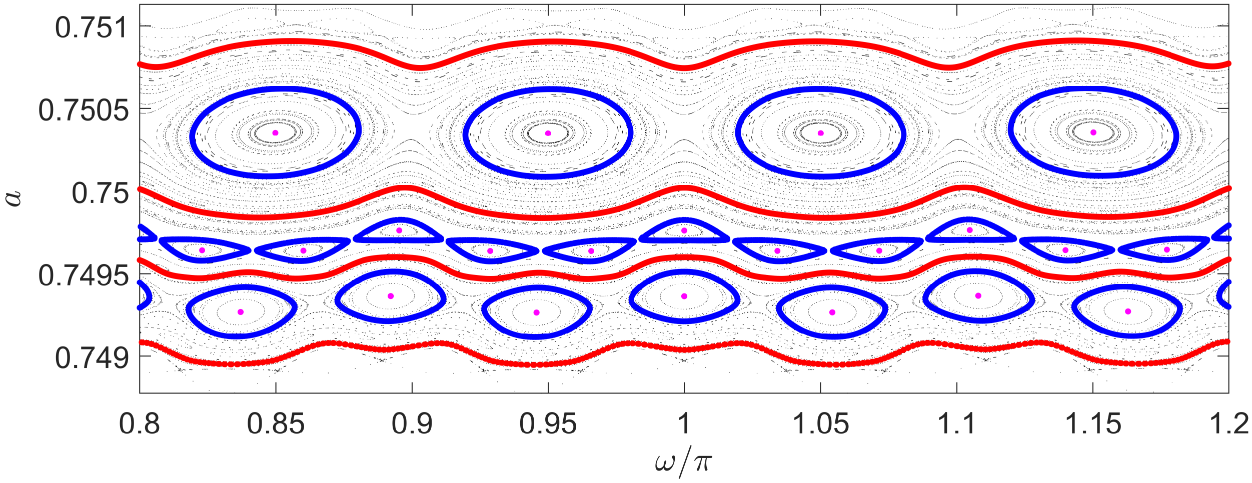

Figure 3.2: Several periodic (magenta) and quasiperiodic (red, blue) trajectories shown over a small portion of phase space. (This behavior indeed extends across the cylinder.) The periodic trajectories comprise elliptic fixed points and, in order of appearance from top to bottom, are 20, 57, and 37-cycles. Respectively, these periodic orbits are of order 6, 20, and 13. They are surrounded by a family of librational circles (outlined in blue). The corresponding hyperbolic points are not shown. Bounding each family of librational circles is a family of rotational circles (outlined in red), or RICs. Note that each region bounded by RICs is isolated from the others.

3.2 How to detect RICs

Various methods have been developed and popularized within celestial mechanics recently to identify and classify parts of the phase space. Such methods, including the finite time Lyapunov exponent (FTLE) and fast Lyapunov indicator (FLI), have proven successful for characterizing/quantifying just how chaotic certain regions are [4, 8, 18]. However, these tools proved not to be appropriate here in identifying RICs. As previously stated, RICs of symplectic twist maps on the cylinder are known to be continuous functions due to a theorem of Birkhoff [12]. This property enabled further ideas such as fractal dimension and continuity tests. Similarly to the FTLE and FLI fields, calculating the fractal dimension was also not an appropriate tool to use; checking for continuity, however, was.

From a numerical perspective, the simple vertical line test is difficult to implement. Each point in the trajectory would require a bin to check for vertical neighbors. Choosing a bin

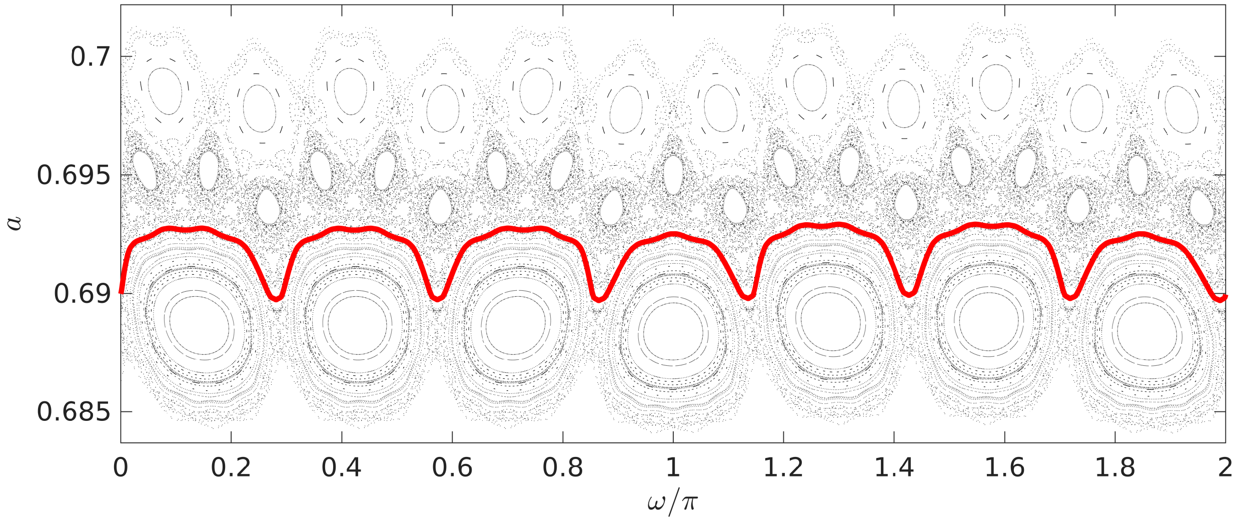

Figure 3.3: An identified RIC in the (ω, a) phase space.

width too small could make a non-function (e.g. librational circle) pass the vertical line test, whereas one too large could make a legitimate function (e.g. an RIC) fail. Therefore, each trajectory is *treated* like a function and checked on its smoothness. This means that trajectories will be sorted (according to the ω coordinate) and checked if $a'(\omega)$ is smooth.

Periodic orbits may be easily identified, but are not nearly as common as quasiperiodic and chaotic trajectories since they have no measure in the phase space. Hence, a periodic orbit will not result from a set of trajectories generated by iteration of randomly selected initial conditions, almost surely. Sifting through chaotic and quasiperiodic trajectories, however, poses more of a challenge in identifying RICs.

Most chaotic trajectories are easily eliminated from RIC contention, though some do have close resemblance when passing nearby a family of RICs (see Figure 3.4). Quasiperiodic orbits tend to be more difficult as they include both RICs and *cantori* (which are made of librational circles); the two become distinguishable from each other given a sufficient number of iterations. In this regard, the complication of these "phantom RICs" tends not to be problematic due to sufficient development of librations and chaotic regions (see Figure 3.5).

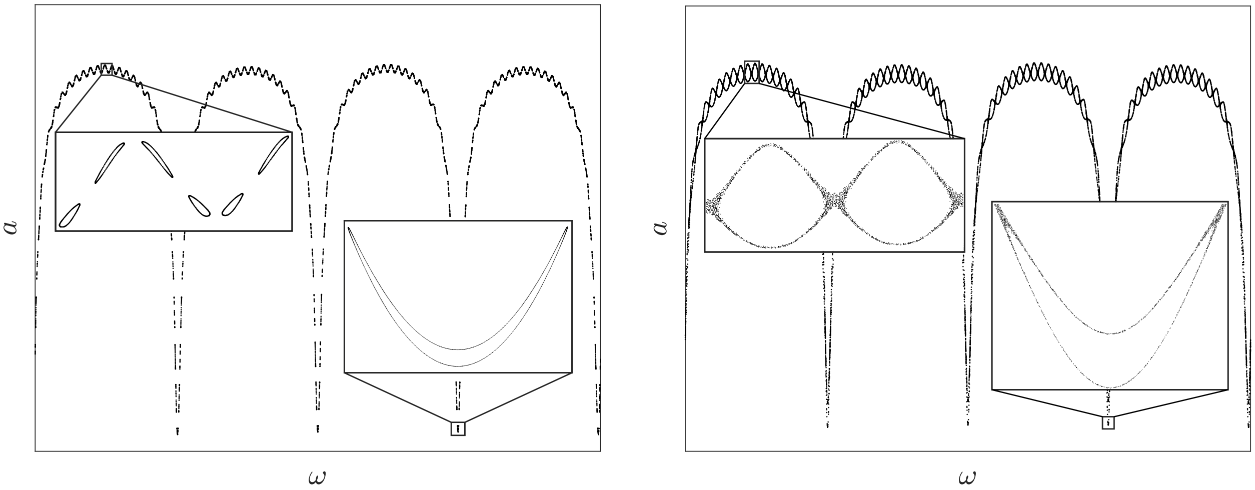

Figure 3.4: **Left:** A cantorus. Each librational circle lies on a smooth curve which, when viewed all together, appear to fill out a graph, but they do not. **Right:** Similar, but chaotic. The regions have a thickness and becomes especially fuzzy near each separatrix. In cases where orbits are sparse or librations are stretched exceptionally thin, the cantorus is generally more difficult to rule out as an RIC.

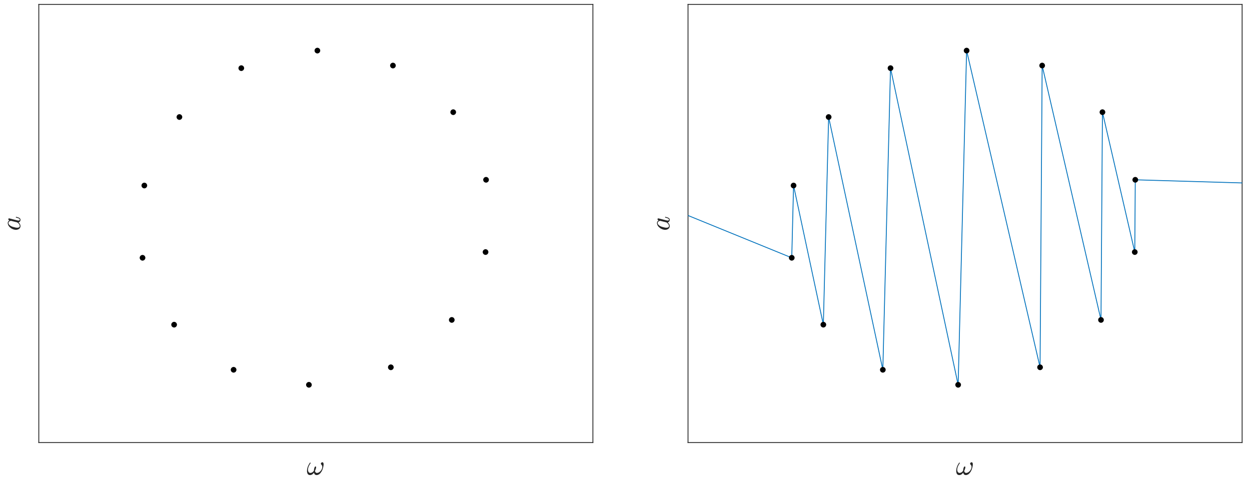

Figure 3.5: **Left:** Librational circle under iterates of the map. **Right:** The same librational circle, but now treated as the function $a = a(\omega)$.

3.2.1 A method to identify RICs

The RIC test is implemented as follows. To be identified as an RIC, a given trajectory $T^N_{(\omega_0,K_0)}$ (with N large and $|K_0 - \bar{K}| < \delta$, where δ is small to establish accuracy of trajectories near the reference orbit) treated as a function must:

- not exceed a specified extent of excursion $\mathcal{E}_{\max}$
- not exceed a specified arc length $\ell_{\max}$
- be continuous and smooth

Note that the first two conditions are added only to provide aide to the third. In practice, both $\mathcal{E}_{\max}$ and $\ell_{\max}$ (which scale with the mass parameter μ for a fixed Jacobi constant C_J) are chosen very large as to not hinder RIC seeking while quickly eliminating obviously non-RIC trajectories. Checking for smoothness is slightly complicated since N is finite. For example, if N is too small, then regions of a quasiperiodic trajectory could be disjointed resulting in leaps/gaps, illustrated in Figure 3.6, which can be difficult to detect.

To begin, the extent of the excursion

$$\mathcal{E} := \max\{a_n\}_{n=0}^{N} - \min\{a_n\}_{n=0}^{N} \tag{3.1}$$

is calculated first since this operation is the quickest; the trajectory is immediately discarded if $\mathcal{E} > \mathcal{E}_{\max}$. Otherwise, the arc length is then calculated using **sorted** coordinates.

$$\ell := \sum_{n=0}^{N-1} \sqrt{(\omega_{n+1} - \omega_n)^2 + (a_{n+1} - a_n)^2} \tag{3.2}$$

Similarly, the trajectory is immediately discarded if $\ell > \ell_{\max}$. Note that the width of the phase space is 2π and RICs will generally be curved (i.e. not straight lines for $\mu > 0$), so $\ell_{\max}$ should accordingly be chosen like $2\pi k$ for some $k > 1$. Chaotic trajectories are susceptible to both extent and arc length, even when $\mathcal{E}_{\max}$ and $\ell_{\max}$ are chosen large, so these two tests alone are both fast and reliable for eliminating trajectories in highly chaotic regions.

Supposing the trajectory has passed these tests, it's now treated like a function with a derivative. As such, single point failures are no longer allowed to accommodate for the possibility of gaps in the dataset as described in Figures 3.4 and 3.6. To expand upon the condition of being continuous and smooth, the trajectory must:

- not exceed a specified number of sign changes in its gradient $N_{\pm\nabla}$
- not exceed a specified gradient $\nabla_{\max}$ a specified number of times $N_{\nabla_{\max}}$
- not exceed a specified "walking angle" $\Theta_{\max}$ a specified number of times $N_{\Theta_{\max}}$

Similar to before, all five parameters should be chosen quite large to allow RICs to pass easily while denying librational circles and phantoms. The first two tests are easily carried out after computing the gradient $a'(\omega)$ by simply counting the number of changes in its sign ($n_{\pm\nabla}$) and amount of times the gradient exceeds its threshold ($n_{\nabla_{\max}}$). Explicitly, these

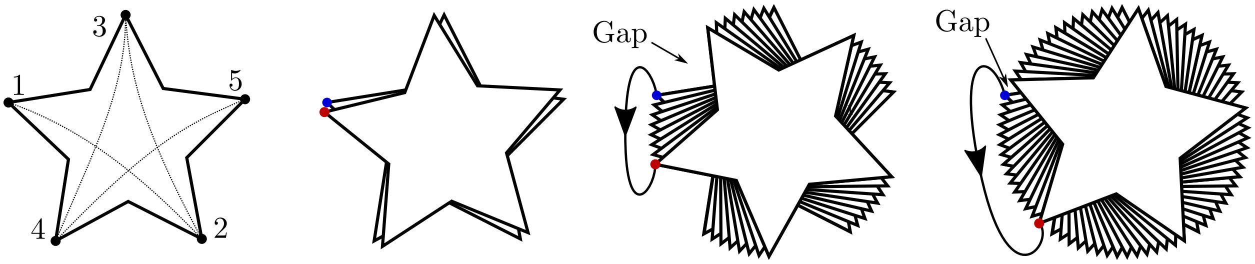

Figure 3.6: A quasiperiodic trajectory represented as the outer points of a star (shown to guide the eye) that returns close to its initial condition after five iterates. The initial condition is marked as blue and its return after performing an excursion is shown in red. Multiple excursions lead to regions that become filled with iterates separated by gaps. These gaps continue to narrow; for a large amount of excursions, the regions become indiscernible from one another as they densely pack together. This star evolution can be viewed as a trajectory *on* the cylinder (librational circle) and iterates of the angle *around* the cylinder (RIC). Note that when viewed on the cylinder, iterates tend to overlap themselves *before* the regions encounter each other for the first time (i.e. the initially large gap "closes").

quantities are

$$\begin{aligned} n_{\pm\nabla} &:= \#\{a : a'(\omega) = 0\} \\ n_{\nabla_{\max}} &:= \#\{a : |a'(\omega)| > \nabla_{\max}\} \end{aligned} \tag{3.3}$$

Due to the extreme oscillatory nature that RICs could have in this map, $N_{\pm\nabla}$ is typically taken as $N_{\pm\nabla} = pN$, where now $p \in (0,1)$ (the percentage of total iterates) is the parameter to choose. These two tests are also quick, so the trajectory is discarded before moving onwards if either $n_{\pm\nabla} > N_{\pm\nabla}$ or $n_{\nabla_{\max}} > N_{\nabla_{\max}}$.

Trajectories making it this far undergo the third and final test above before being declared an RIC. This test checks for continuity using an angle approach, which assists in vetting trajectories that may have evaded the gradient test by using an additional piece of information from that of forward finite difference.

Let $\mathbf{v}_1$ and $\mathbf{v}_2$ be vectors as depicted in Figure 3.7.

$$\mathbf{v}_1 = \begin{bmatrix} x_{n+1} - x_n \\ y_{n+1} - y_n \end{bmatrix} = \begin{bmatrix} \Delta x_1 \\ \Delta y_1 \end{bmatrix} \quad \text{and} \quad \mathbf{v}_2 = \begin{bmatrix} x_{n+2} - x_n \\ y_{n+2} - y_n \end{bmatrix} = \begin{bmatrix} \Delta x_2 \\ \Delta y_2 \end{bmatrix} \tag{3.4}$$

Then the angle $2\theta_n \in (0, \pi)$ between these two vectors follows from a cross product.

$$\sin\theta_n = |\hat{\mathbf{v}}_1 \times \hat{\mathbf{v}}_2| = \frac{|\Delta x_2 \Delta y_1 - \Delta x_1 \Delta y_2|}{\sqrt{(\Delta x_1^2 + \Delta y_1^2)(\Delta x_2^2 + \Delta y_2^2)}} \tag{3.5}$$

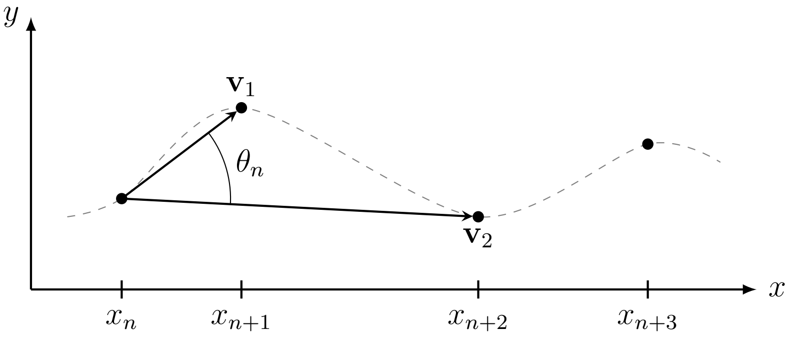

Figure 3.7: Defining the angle θ_n made between the vectors pointing to the next two neighboring points, x_{n+1} and x_{n+2}, from the current point x_n for arbitrary data in the (x, y) plane. The question to address is whether this data set lies on some differentiable curve (shown dashed) or not.

Remark 3.1. If this data set is representative of a differentiable function such that $y = f(x)$ for any such function $f \in C^1$, then $\theta_n \to 0$ as $\Delta x_1, \Delta x_2 \to 0$.

Proof. Let $\Delta x_1 = \epsilon > 0$ and $\Delta x_2 = 2\Delta x_1 = 2\epsilon$. Suppose $y = f(x)$, where $f \in C^1(\mathbb{R})$ is a differentiable function. Then

$$\sin\theta_n = \frac{|2\epsilon\Delta y_1 - \epsilon\Delta y_2|}{\sqrt{(\epsilon^2+\Delta y_1^2)(4\epsilon^2+\Delta y_2^2)}} = \frac{1}{\epsilon}\frac{|2\Delta y_1 - \Delta y_2|}{\sqrt{(1+(\Delta y_1/\epsilon)^2)(4+(\Delta y_2/\epsilon)^2)}}.$$

Now, $\Delta y_1 = f(x_n+\epsilon) - f(x_n)$ and $\Delta y_2 = f(x_n+2\epsilon) - f(x_n)$ so that

$$\begin{aligned} 2\Delta y_1 - \Delta y_2 &= 2\big(f(x_n+\epsilon) - f(x_n)\big) - \big(f(x_n+2\epsilon) - f(x_n)\big) \\ &= f(x_n+\epsilon) - f(x_n) - \big(f(x_n+2\epsilon) - f(x_n+\epsilon)\big). \end{aligned}$$

Hence,

$$\sin\theta_n = \frac{\left|\frac{f(x_n+\epsilon)-f(x_n)}{\epsilon} - \frac{f(x_n+2\epsilon)-f(x_n+\epsilon)}{\epsilon}\right|}{2\sqrt{\left(1+\left(\frac{f(x_n+\epsilon)-f(x_n)}{\epsilon}\right)^2\right)\left(1+\left(\frac{f(x_n+2\epsilon)-f(x_n)}{2\epsilon}\right)^2\right)}}.$$

Particularly, letting the neighboring points become arbitrarily close to one another provides

$$\lim_{\epsilon\to 0}\sin\theta_n = \frac{1}{2}\frac{|f'(x_n) - f'(x_n)|}{1+f'(x_n)^2} \equiv 0$$

which implies $\theta_n \to 0$ as $\epsilon \to 0$. □

Because of quasiperiodicity, iterates on an RIC both fill out a differentiable curve and get arbitrarily close to one another. Hence, the θ signature of an RIC should remain small when highly iterated ($N \gg 1$) with peaks most probably occurring near regions of high curvature. Likewise, iterates of librations/cantori and chaotic trajectories should be highly jagged with frequent, large spikes. Thus, the amount of spikes exceeding the threshold ($n_{\Theta_{\max}}$) is counted; explicitly with θ_n defined as in (3.5),

$$n_{\Theta_{\max}} := \#\{\theta : \theta > \Theta_{\max}\}. \tag{3.6}$$

As with the other two tests here, the trajectory is rejected if $n_{\Theta_{\max}} > N_{\Theta_{\max}}$.

3.3 Results

The algorithm described above was implemented over 83 mass parameters $\mu \in [10^{-8}, 10^{-3}]$ with $C_J = 3$ using the interior Keplerian map. Through trial and error, the threshold values were selected according to Table 3.1. A first RIC was identified in each system and its average semimajor axis was calculated through quadrature; the chaotic zone could then be estimated as the distance between the secondary and apoapse.

$$a_{\text{RIC}} := \frac{1}{2\pi}\int_{S^1} a(\omega)\, d\omega, \qquad r_{\text{RIC}} := 1 - a_{\text{RIC}}(1 + e_{\text{RIC}}) \tag{3.7}$$

Here, e_{RIC} follows from the Tisserand parameter (2.12).

When plotted on a log-log scale as in Figure 3.8, the overall trend of the RIC radius follows a power law distribution. Applying this fit in the sense of least squares obtains

$$r_{\text{RIC}} \approx 0.6997\mu^{0.2417}. \tag{3.8}$$

This appearance of the first RIC gives a new definition of the planetary zone radius, where we note this measure naturally takes into account that three-body dynamics are along energy

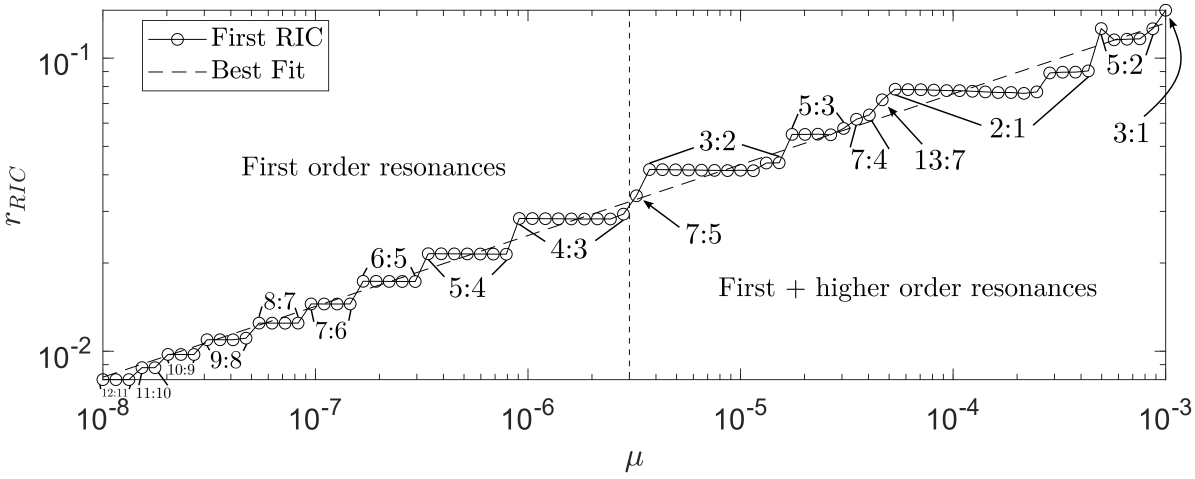

Figure 3.8: Growth of the distance from the primary during close approach for which energy kicks cease to provide meaningful transit.

Table 3.1: Chosen parameters for detecting RICs.

N	δ	$\mathcal{E}_{\max}$	$\ell_{\max}$	$\nabla_{\max}$	$\Theta_{\max}$	$N_{\pm\nabla}$	$N_{\nabla_{\max}}$	$N_{\Theta_{\max}}$
10^4	0.0025	0.025 to 0.050	4π	5	15°	4000	50	50

surfaces — in this case, the Tisserand curve in (a, e) space where $\mu \ll 1$. This RIC boundary is the largest McGehee torus, which blocks transport between the primary and secondary for low enough energies [11]. From Figure 3.8, the first emerging RICs appear in families surrounding *first*-order mean motion resonances in the (ω, a) phase space for $\mu \lesssim 3 \times 10^{-6}$. For increasing μ from here, such families are detected at second and higher order resonances in between the first-order resonances.

These first emerging RICs exhibit step-like behavior because the perturbation strength μ must fully destroy the RIC families lying outside of the resonance zone before chaotic trajectories can traverse through it. Generally, each step is slightly tilted downwards for increasing μ since the family is pushed upwards when being destroyed. This behavior is seen

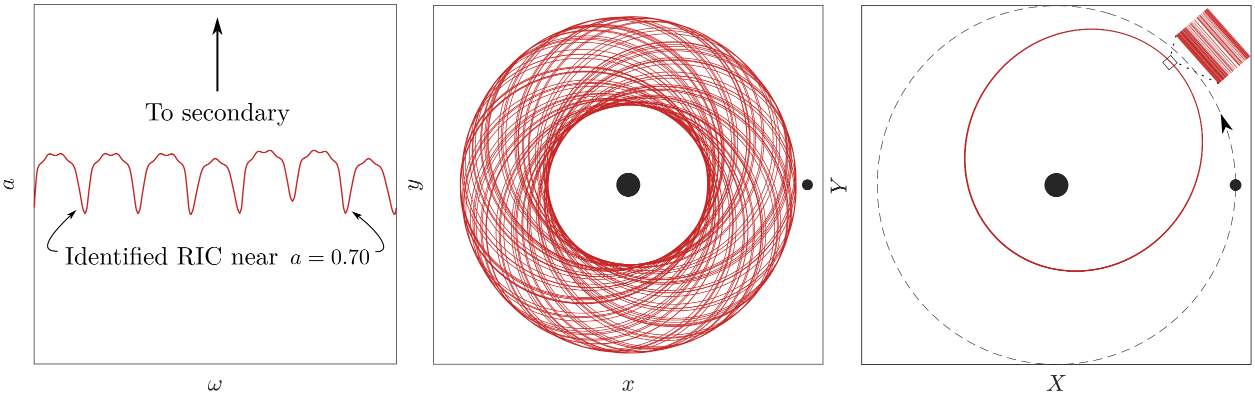

Figure 3.9: **Left:** The first RIC in the interior Keplerian map with $\mu = 3.5 \times 10^{-5}$ and $C_J = 3$ (corresponding to the 7 : 4 resonance of Figure 3.8), which forms a continuous curve around the cylinder. **Middle:** The trajectory in the rotating frame. Note that because the RIC is a continuous curve, this is actually a densely filled annulus (which is the projection of the McGehee torus into configuration space). The chaotic zone r_{RIC} is the distance between this invariant surface's (average) outer boundary and the secondary. **Right:** The trajectory in the inertial frame; the elapsed time at the current iteration, required to transform into the inertial frame, is given by (2.22). The particle falls into a wobbling, frozen-like orbit due to the RIC's quasiperiodicity.

in the bifurcation sequence in Figure 3.10. Some steps shown, such as the 4 : 3, 3 : 2, 5 : 3, and (most distinctively) 2 : 1 resonances, have a slight increase in their RIC radius before moving onto the next step. These correspond to the “strong” RICs below the resonance still existing after the “weak” RICs above the resonance have already been destroyed. The RICs above and below the resonance therefore do not bifurcate symmetrically, but the strong ones are close to follow.

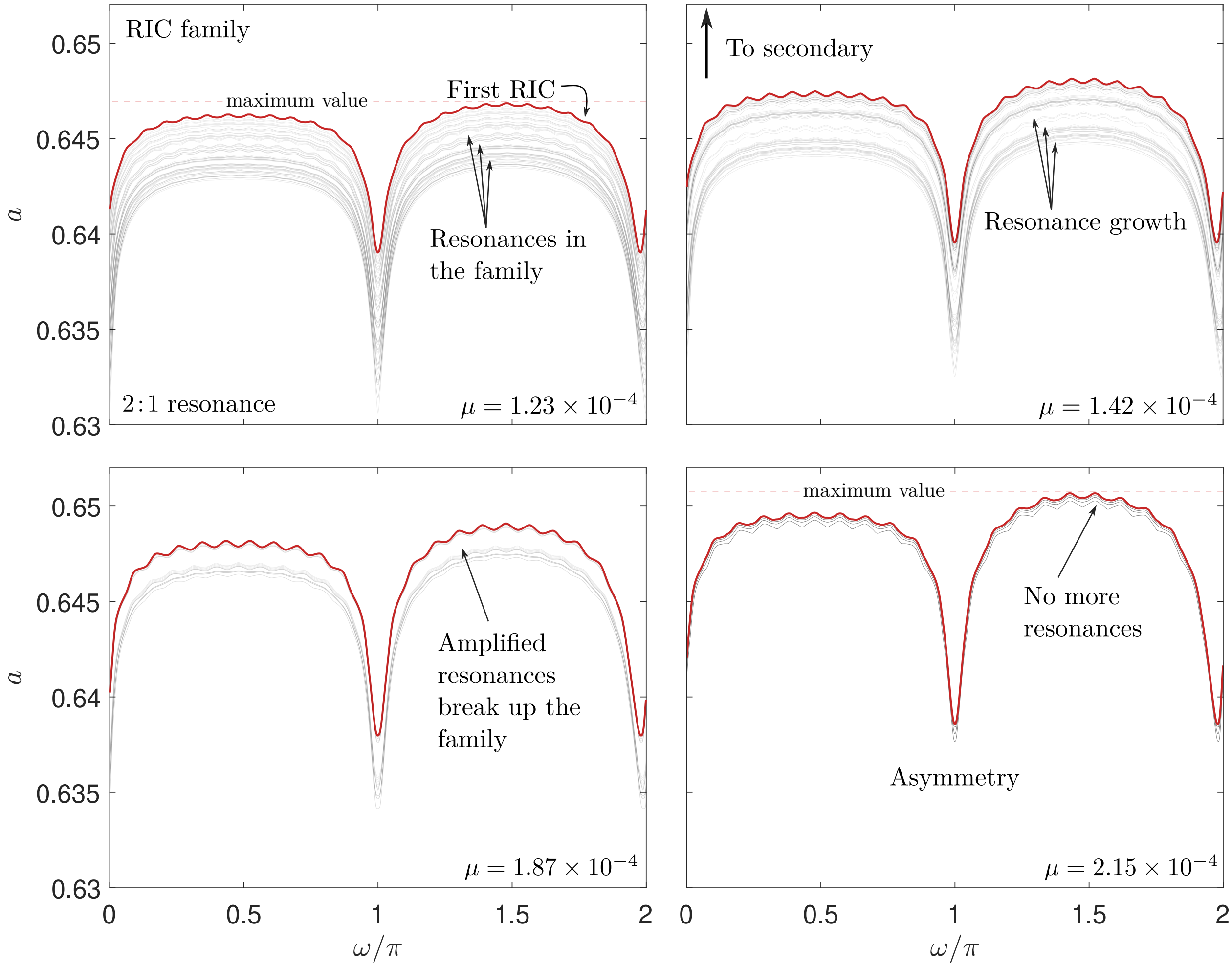

Figure 3.10: Evolution of RIC families above the 2 : 1 resonance as μ increases from 1.23×10^{-4} (top left) to 2.15×10^{-4} (bottom right). In this progression, the families become thinner and are pushed upwards, away from the hyperbolic fixed point located around $(\omega, a) = (\pi, (1/2)^{2/3})$. This behavior is generic for other $s : r$ resonances.

3.3.1 Comparison to other chaotic zones

A short comparison to other more well known and established chaotic zones is in order. The smallest measure for a radius of significant influence around the secondary is the sphere of influence (SOI) followed by the Hill sphere [1, 13, 17]. Both are obtained by equating gravitational/centrifugal forces to find the separating region where one body has more influence on the particle than the other. A more closely related chaotic zone from Wisdom [20] measures the radius of first-order mean motion resonance overlap. Wisdom's estimate is done for initially circular orbits (i.e., confined to $e = 0$ initially in (a, e) space), which differs from the RIC estimate in that the extent of the chaotic zone is described along the energy surface provided by the Tisserand parameter (2.12) in (a, e) space instead of along the a-axis. The resonance (RIC and Wisdom) estimates are in fair agreement from Figure 3.11; both lie far above the SOI and Hill zones obtained from force balancing. It is noted that there is a crossing between the resonance estimates at $\mu \sim 1.3 \times 10^{-6}$.

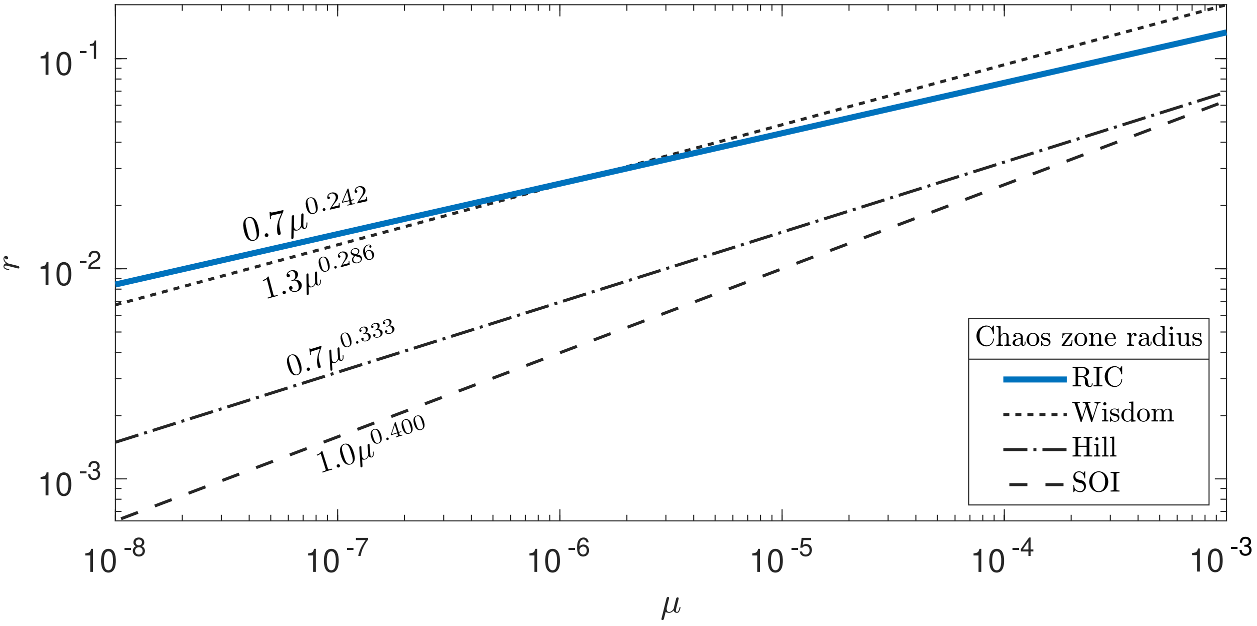

Figure 3.11: Comparison of the RIC radius to other chaotic zone estimates.

An interesting parallel to the Hill radius, expressed $(\mu/3)^{1/3}$, could be drawn from the RIC radius (3.8) as it looks similar to $(\mu/4)^{1/4}$. This claim could be refined by repeating the calculation with μ more resolved, varying the Tisserand parameter C_J, and complementing these results (of the interior map) with an estimate for the exterior Keplerian map.

Chapter 4

Multibody transfer

Finding a trajectory (in continuous-time) that successfully completes a transfer between masses in the restricted 4-body problem, say m_2 and m_3 as shown in Figure 2.1a, is rightfully challenging and time-consuming — especially so when employing methods like differential correction. The Keplerian map, however, provides an alternative, much faster way to determine if the transfer is even possible (via RICs) and identify regions of phase space susceptible to transfer, thus providing guesses of initial conditions that can then be iterated upon by differential correction. It is enacted in the PCCR4BP, shown in Figure 2.1b, where the mass parameter for each three-body system is assumed small enough that the central body m_1 is considered stationary at the origin.

The procedure of finding a transfer, supposing it exists, is as follows. First, the particle must be able to transition between the two systems using a switching orbit via the Tisserand curve of Figure 2.5. A reference orbit, along which to evaluate the Keplerian map for symplecticity, is then established between the manifold trajectories of Section 2.2.2 and the switching orbit. Initial conditions are populated about the reference orbit and iterated in the appropriate direction until reaching (a neighborhood of) the switching and manifold orbits in each system. A pair of trajectories, one from each system, reaching both the switching region and the manifold region is a *transfer trajectory.* Finding a transfer trajectory in discrete time provides an initial guess for initial conditions in continuous time which could then be refined and brought into more perturbed models through continuation.

4.1 Switching between systems

Without loss of generality, let one of the two 3BPs be a distance 1 from the central body. Viewing the transfer in forward time, this system is referred to as the *departure system*. The remaining 3BP, a distance $A > 0$ from the primary (in the departure system's units), is therefore called the *capture system*.

The particle admits a Jacobi constant and associated Tisserand parameter in each 3BP system. Figure 2.5 indicates that, when expressed in consistent units, there can be an intersection with appropriately chosen values. This intersection provides the switching orbit as seen in Figure 4.2 — the point at which the particle can move between being controlled by one 3BP system to the other. In principle, these Tisserand parameters can be independent from one another, but we take them both to be the same (i.e., $C_{J1} = C_{JA} = C_J$) for simplicity. In this case, the switching orbit between the departure system and capture system of distance $A > 0$ from the central body is given by

$$\begin{aligned} a_{\text{switch}} &:= \frac{1 + \sqrt{A} + A}{C_J} \\ e_{\text{switch}} &:= \sqrt{1 - \frac{C_J^3}{4} \frac{(A - \sqrt{A})^2}{(A - \sqrt{A} + 1)^3}}. \end{aligned} \tag{4.1}$$

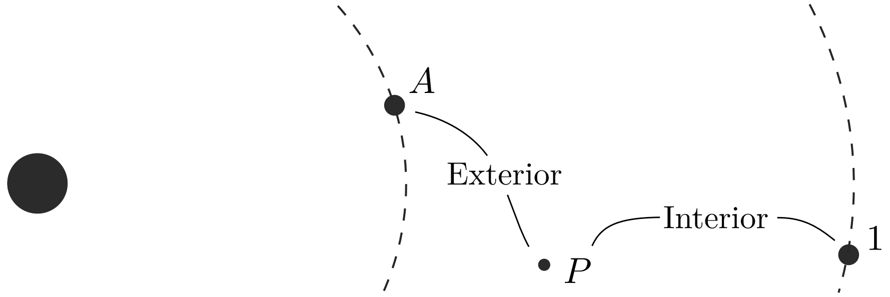

Figure 4.1: Dimensionalization of one 3BP system in terms of the other. In this configuration, the particle's motion is interior to the departure system (labelled a distance 1 from the primary) and, similarly, exterior to the capture system (A). Note that the capture system is still a unit distance away from the primary in its *own* system (the other body being $1/A$).

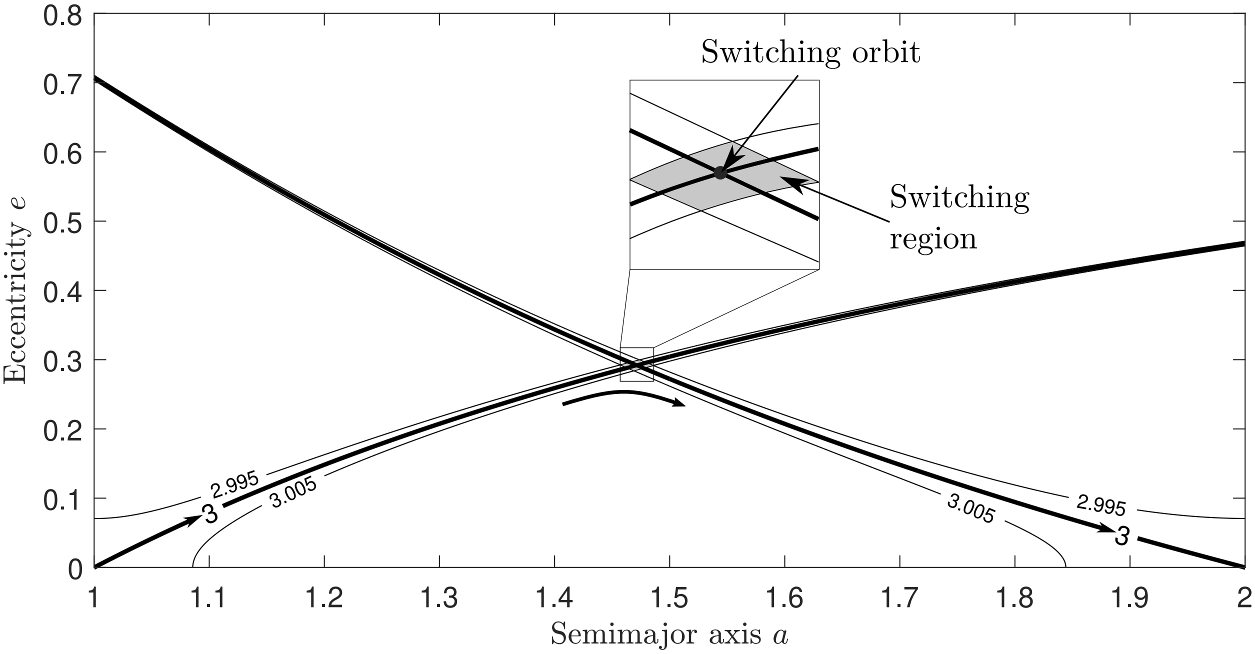

Figure 4.2: Tisserand curves from two 3BP systems with a chosen Jacobi constant C_J and distance A intersect at a switching orbit. The switching orbit is closely surrounded by other potential switching orbits for slightly different Jacobi constants, forming a switching region. The switching orbit provides the means for the particle to switch being dominated by one 3BP system to the other. Here, the switching orbit is parameterized by $A = 2$ and $C_J = 3$.

4.1.1 Preliminary energetic bounds

To a zeroth-order approximation (i.e., ignoring the manifolds of the Lagrange points), the switching orbit (4.1), geometrically described by the parameters (a, e), should be contained within the two systems of $(a, e) = (1, 0)$ and $(a, e) = (A, 0)$. Knowing $0 < e < 1$ provides preliminary bounds for C_J in terms of the geometry induced by the distance A.

$$0 < C_J < \underbrace{2^{2/3} \frac{1 + \sqrt{A} + A}{(\sqrt{A} + A)^{2/3}}}_{\text{minimum value: 3}} \tag{4.2}$$

This suggests that there is an energy interval for which transfers over the distance $|1 - A|$ are feasible. In other words, the particle can only be so energetic in the Keplerian map before a transfer becomes impossible, at least in the sense of a sensible switching orbit. While both bounds are rather weak, they still provide useful information (e.g., $C_J > 0$).

Improvements on the bounds are made by knowing that the eccentricity cannot approach 1 (accordingly, the Jacobi constant cannot approach 0) since the switching orbit must be bounded between the departure and capture orbits. To the same zeroth-order approximation, the switching orbit is therefore bounded between the two bodies. That is, the inequalities $A < q_{\text{switch}} < Q_{\text{switch}} < 1$ for $A \in (0,1)$ and $1 < q_{\text{switch}} < Q_{\text{switch}} < A$ for $A \in (1,\infty)$ with $A > 0$ some fixed distance must be satisfied for a suitable switching orbit. Here, $q = a(1-e)$ and $Q = a(1+e)$ are the periapse and apoapse distances, respectively. The requirements may be reduced in each case upon plotting these four constraints (implicit functions of A and C_J); one inequality automatically satisfies the other for all respective values of A.

$$\begin{cases} a_{\text{switch}}(1-e_{\text{switch}}) > A, & (0 < A < 1) \\ a_{\text{switch}}(1-e_{\text{switch}}) > 1, & (1 < A < \infty) \end{cases}$$

Let $C_J^{\text{intersect}}$ denote the Jacobi constant at which the above inequalities are violated by exact equality (i.e., the switching orbit grazes the bodies). Then

$$\frac{1}{2}C_J^{\text{intersect}} := \begin{cases} \dfrac{1+\sqrt{A}+A}{(1+\sqrt{A})^2}\left(\sqrt{A^2+2(1+\sqrt{A})^2}-A\right), & (0 < A < 1) \\ \dfrac{1+\sqrt{A}+A}{(\sqrt{A}+A)^2}\left(\sqrt{1+2(\sqrt{A}+A)^2}-1\right), & (1 < A < \infty) \end{cases} \tag{4.3}$$

which improves the lower bound of the Jacobi constant ($0 < C_J^{\text{intersect}} < C_J$). By this measure, an absolute minimum for the Jacobi constant is admitted as $\sqrt{8} \approx 2.83$, a statement that the particle can only be so energetic for the transfer to be possible. Note that the result for $A < 1$ is simply the result for $A > 1$ under the mapping $A \mapsto 1/A$ as necessitated by symmetry. The lower bound may be further refined by considering geometric constraints of the reference orbits.

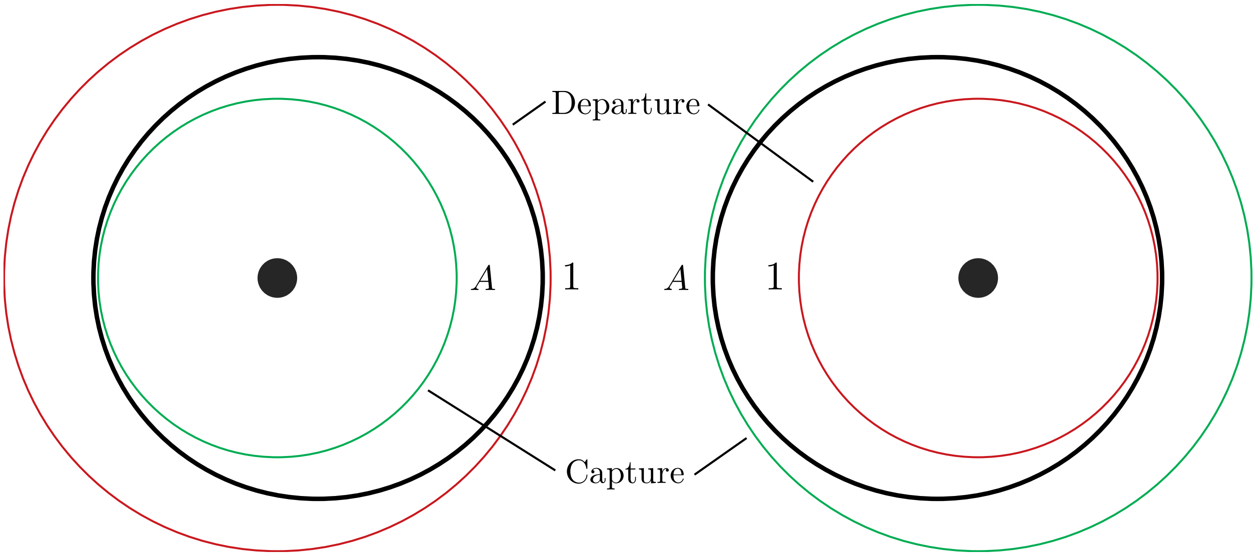

Figure 4.3: The switching orbit lies in between the departure ($a \sim 1$) and capture ($a \sim A$) orbits. Its Tisserand parameter should be chosen such that it has close approaches to *both* systems. Not enough energy (too large of a Jacobi constant) pulls the switching orbit away from the bodies; too much energy (too low of a Jacobi constant) pushes the switching orbit too close to the bodies since it intersects their trajectories.

4.2 Symplecticity through reference orbits

Recall that the Keplerian map is parameterized about the reference orbit with geometry $(\bar{a}, \bar{e})$, where $\bar{e}$ is induced by the Tisserand parameter C_J (2.12), so that $a_1 < \bar{a} < a_2$ by (2.24) for motion along $C_J = \text{const}$. The switching orbit provides a boundary on the extent to which the particle can transit in each system, which means that the semimajor axes a_1 and a_2 are determined by the body's switching and manifold (of Section 2.2.2) orbits.

Let $(\bar{a}_1, \bar{e}_1)$ and $(\bar{a}_A, \bar{e}_A)$ denote the departure and capture systems' reference orbits (all expressed in the departure system's units), respectively. Then to the same zeroth-order approximation of the manifolds and with $C_J = \text{const.}$ between each system,

$$\bar{a}_1 = \lambda + (1-\lambda)a_{\text{switch}}, \qquad \bar{a}_A = \lambda A + (1-\lambda)a_{\text{switch}}. \tag{4.4}$$

Note that $\bar{e}_A$ should be evaluated using $\bar{a}_A$ in its own system's units (i.e., using $\bar{a}_A/A$).

4.2.1 Refining the energetic bounds

Similar to before, the manifold orbits may be estimated to zeroth order as the bodies themselves so that departure becomes $(a, e) \approx (1, 0)$ and capture likewise $(a, e) \approx (A, 0)$. In this case, each reference orbit simply must fit between the secondary's orbit and the switching orbit. Doing so will provide a further tightening on the bounds on possible Jacobi constants C_J as a function of the mixing parameter λ.

To ensure that the reference orbits fall within their respective geometric bounds, the inequalities $A < \bar{q}_A < q_{\text{switch}} < \bar{Q}_A \lesssim \bar{q}_1 < Q_{\text{switch}} < \bar{Q}_1 < 1$ for $A \in (0, 1)$ must be obeyed. The inequalities follow similarly for $A \in (1, \infty)$; that is, they are the same as above but with $A \rightleftharpoons 1$. In each of the two scenarios, the inequalities explicitly involving the switching orbit are automatically satisfied by the others. With $q < Q$ trivially, the set thus reduces to

$$\begin{cases} A < \bar{a}_A(1 - \bar{e}_A) \quad \text{and} \quad \bar{a}_1(1 + \bar{e}_1) < 1, & (0 < A < 1) \\ 1 < \bar{a}_1(1 - \bar{e}_1) \quad \text{and} \quad \bar{a}_A(1 + \bar{e}_A) < A, & (1 < A < \infty). \end{cases}$$

Further, only one constraint is needed for mixing parameters $\lambda \gtrsim 0.3$ determined graphically.

For simplicity, choose $\lambda = 0.5$ so that the reference orbit takes the average semimajor axis of the body and the switching orbit. Doing so corresponds to about midway along each Tisserand curve of Figure 4.2. Under this choice, the lower bound of the Jacobi constant for a given capture distance A such that the trajectory geometries do not intersect each other is given implicitly as $F = 0$, where $F : \mathbb{R}^2 \to \mathbb{R}$ is given by

$$F := \begin{cases} \dfrac{1 + \sqrt{A} + A + C_J}{2C_J} \left(1 + \sqrt{1 - \dfrac{{C_J}^3}{2} \dfrac{(1 - \sqrt{A} - A - C_J)^2}{(1 + \sqrt{A} + A + C_J)^3}} \right) - 1, & (0 < A < 1) \\ \dfrac{1 + \sqrt{A} + A + AC_J}{2C_J} \left(1 + \sqrt{1 - \dfrac{A{C_J}^3}{2} \dfrac{(1 + \sqrt{A} - A + AC_J)^2}{(1 + \sqrt{A} + A + AC_J)^3}} \right) - A, & (1 < A < \infty). \end{cases} \tag{4.5}$$

For numerical implementation requiring higher precision, it may be better to solve the initial value problem

$$\frac{dC_J}{dA} = -\left(\frac{\partial F}{\partial C_J}\right)^{-1}\frac{\partial F}{\partial A}, \qquad C_J(1) = 3. \tag{4.6}$$

In practice, the initial condition cannot be exactly 3, but a close approximation of 3 works just as well. This curve, forming a new lower bound for Jacobi constants C_J, is shown in Figure 4.4. An example set of switching and reference orbits is shown in Figure 4.5. These lower bounds rely only upon the geometry induced by A; specifically, they do not involve the dynamics of the L_1 and L_2 neck regions governed by the mass parameter μ in either system. However, the bounds naturally maximize themselves at $C_J = 3$ corresponding to the energy interval of Figure 2.3 without zero-velocity curves. Hence, it should be ensured that the orbits are nested *and* the appropriate neck regions are open if $C_J > 3$.

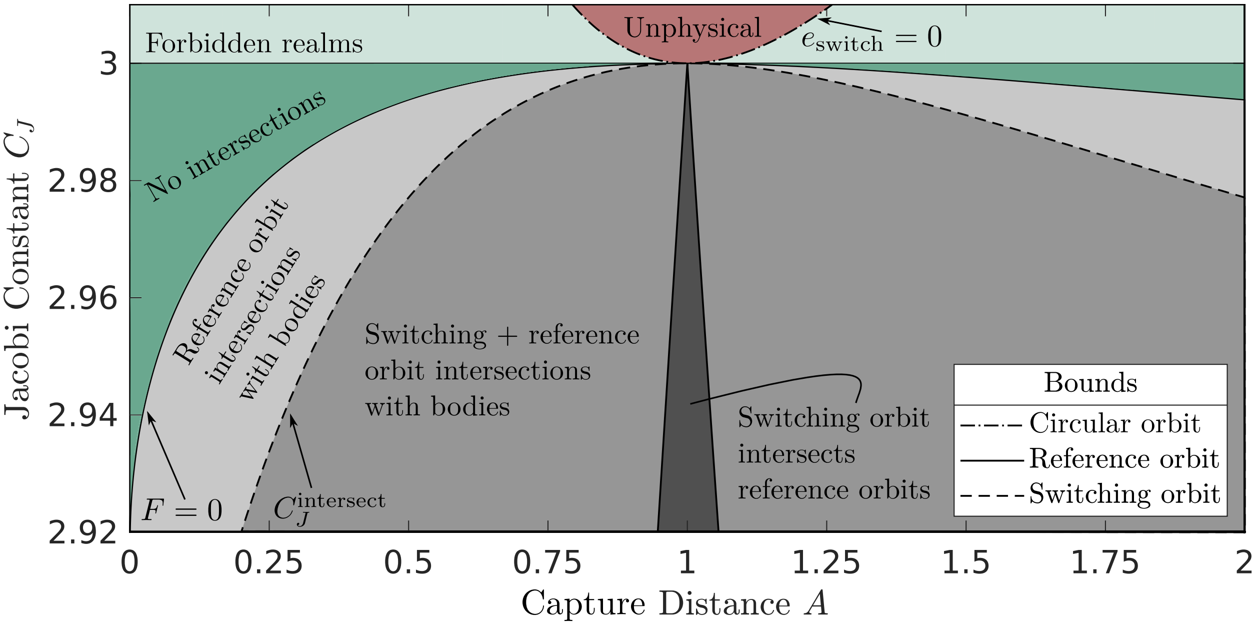

Figure 4.4: Improvement of the lower bounds for the Jacobi constant so that the reference orbits are nested between the bodies and the switching orbit for $\lambda = 0.5$. The green regions have no intersections between any orbits (to zeroth order in μ), so they serve as a good place to select a Jacobi constant for a given body with semimajor axis $a = A$. The grey regions can be selected, but the choice will likely not be as good because orbits will be intersecting each other to varying degrees of badness. The red region cannot be selected because it violates the constraint $0 < e < 1$.

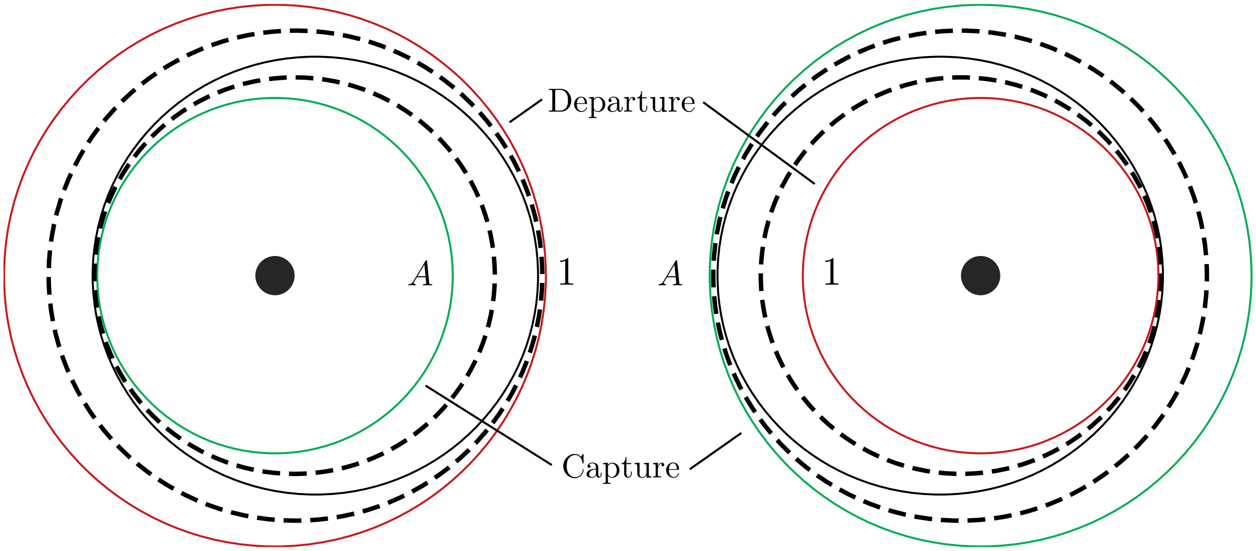

Figure 4.5: The reference orbits (dashed) lie in between the departure/switching and capture/switching orbits. None of the curves intersect each other which means this Jacobi constant is admissible by Figure 4.4 (here $A = 1.5$, $C_J = 3$, and $\lambda = 0.5$). The switching orbit provides a means to exit one system while entering into the other; each reference orbit typically gets squeezed between the switching orbit and the perturbing body.

4.3 Finding transfer trajectories

Using the reference orbits to parameterize the kick functions, trajectories in each of the two systems can now be established. Of particular interest are those trajectories in each of the two systems that include the manifold *and* switching orbits. Suppose there are no RICs blocking transport, corresponding to the particle's close approach remaining within the secondary's chaotic zone, so that a transfer is possible. Then in each system, we wish to find initial conditions (ω_0, K_0) of a trajectory $T^{M,N}_{(\omega_0,K_0)}$ that does the following:

- For some $M \in \mathbb{Z}$, $\mathbf{F}^M(\omega_0, K_0)$ lies on the manifold orbit ($|K_M - K_{\text{manifold}}| = 0$).
- For some $N \in \mathbb{Z}$, $\mathbf{F}^N(\omega_0, K_0)$ lies on the switching orbit ($|K_N - K_{\text{switch}}| = 0$).
- The maps are iterated in opposite directions ($MN \leqslant 0$).

The particle transfers from the departure manifold orbit to the capture's manifold orbit in forward time; thus, $M \leqslant 0 \leqslant N$ for the departure system while $N \leqslant 0 \leqslant M$ for the capture system. Equality follows only if the initial conditions are placed *on* the intended orbit.

These two situations ($N = 0$ or $M = 0$) present the simplest configurations of initial conditions. Without loss of generality, consider the initial conditions placed on the switching orbit. In this case, the objective is to find trajectories that transit to each system's manifold orbit under iteration of the Keplerian map. Because the two systems are independent from one another, each trajectory *connects* with the other system regardless of differences in their ω coordinate. Thus, connection trajectories that also include the manifold orbits are considered transfer trajectories.

Computationally, acquiring initial conditions that exactly satisfy the requirements is difficult, so the first two conditions are interpreted to be satisfied within a set tolerance δ. That is, trajectories from each system are still identified as a connection at the switching orbit (likewise at the manifold orbit) if they fall within a δ distance of it.

$$|K_M - K_{\text{manifold}}| < \delta \quad \text{and} \quad |K_N - K_{\text{switch}}| < \delta$$

This relaxation leads to the notion of the *switching region* shown in Figure 4.2; the notion of *manifold regions* follow similarly. Once transfers are found, they can be sorted according to both how closely they match to the switching/manifold orbits and their time of flight (relative to the departure system).

$$\Delta t_{\text{total}} := \underbrace{2\pi \sum_i a_i^{3/2}}_{\text{depart. sys. } \Delta t} + \underbrace{2\pi \sum_j (Aa_j)^{3/2}}_{\text{capture sys. } \Delta t} \tag{4.7}$$

Here, the indices i and j cover all of the iterations in each separate system. The normalization Aa is written for the capture system since the Keplerian map is iterated in self-consistent units for each system. The quantity $\Delta t_{\text{total}}/2\pi$ expresses the duration in terms of how many circuits the departure body has completed over that amount of time (for Earth, "years").

4.3.1 Generating initial conditions

A short discussion on the uniform distribution of initial conditions proceeds. Numerically, truly random numbers can be difficult to obtain quickly and in large quantity; *pseudorandom* numbers are typically used in their stead. Such numbers stem from a *seed* used in an *algorithm*, and the sequence of these numbers is called a *stream*. Each stream is a deterministic sequence generated by the algorithm and the seed. In this regard, the process is analogous to a differential equation, where the seed is the initial condition and the stream is the solution to the system given by the algorithm.

Theoretically, each stream is sufficiently large enough to exhaust all practical desire for random numbers. The stream, however, is killed and the seed reset to its default value (0) at the end of each computing session. To avoid repeated numbers during calculations in the next computing session, one could either recover the stream's position by requesting a sufficient amount of numbers, or simply change the seed.

In practical application, the seed is changed to "ensure" that generated streams are independent from one another. For this work, the seed s is given as

$$s = w\left\lceil \prod t \right\rceil \mod 2^{32}, \tag{4.8}$$

where $t =$ (year, month, day, hour, minute, seconds) is the current time of execution (with hours in the 24^{h} format, seconds including decimals, and the rule that $0 \mapsto 999$) and $w \in \mathbb{N}$ is the worker's index. For single core computations, $w = 1$; otherwise, w is automatically assigned to each worker in the pool. While this formulation does not guarantee a unique seed at any given execution time, the probability of generating a unique seed from (4.8) exceeded 95%, which was found to be sufficient for this work.

4.4 Demonstration of an uncontrolled transfer from Earth to Venus

Using the tools developed for the Keplerian map, a transfer trajectory from Earth to Venus is demonstrated below. It is noteworthy that the following procedure was also applied for an Earth to Mars transfer and one eluded to be found.

4.4.1 Setup

Take Earth to be the departure body and Venus as the capture body, which of course share the sun as the primary body. Because of this choice, the (nondimensional) distances are measured in astronomical units (AU). From this perspective, the **Earth** is located at $(a, e) = (1, 0)$ while **Venus** at $(a, e) = (0.723, 0)$ — that is, $A = 0.723$ AU so that the distance to be transited is $|1 - A| = 0.277$ AU. The **mass parameter** of the Sun-Earth system is $\mu = 3.0035 \times 10^{-6}$ and that of the Sun-Venus system is $\mu = 2.4478 \times 10^{-6}$. Let $C_J = 3$ for the particle's motion along the energy surface (Figure 2.5); all forbidden realms (Figure 2.3) are eliminated and the manifold, reference, and switching orbits do not intersect each other. Thus, this Jacobi constant is admissible.

The departure from Earth occurs in a manner similar to its **unstable manifold** of the Sun-Earth L_1 point which, by (2.15), is described by $(a, e) = (0.962, 0.02962)$. Similarly for Venus, but approaching along the **stable manifold** of the Sun-Venus L_2 point, its manifold orbit is $(a, e) = (1.039, 0.02837)$ — with a in AU, $(0.751, 0.02837)$. The **switching orbit** (4.1) for the Sun-Earth system has the semimajor axis $a_{\text{switch}} = 0.858$; in the Sun-Venus system, $a_{\text{switch}} = 1.187 = 0.858$ AU. The eccentricity is induced by the Tisserand parameter and in both systems is $e_{\text{switch}} = 0.140$. Let $\lambda = 0.5$ so that each **reference orbit** is the

Table 4.1: Summary of the parameters used to define the manifold, reference, and switching orbits for the Sun-Earth and Sun-Venus systems. These two systems are expressed in their *own* units; however, the Sun-Venus* system is expressed in units relative to the Sun-Earth system. The unstable and stable manifolds do not follow the energy surface induced by $C_J = 3$; instead, they have eccentricities $e_{W^u(L_1)} = 2.962 \times 10^{-2}$ and $e_{W^s(L_2)} = 2.837 \times 10^{-2}$. These orbits respectively correspond to Tisserand parameters $C_{JW^u(L_1)} = 3.00027231$ and $C_{JW^s(L_2)} = 3.00027033$.

System	μ	A	C_J	λ	$a_{W^u(L_1)}$	$a_{W^s(L_2)}$	$\bar{a}$	a_{switch}
Sun-Earth	3.0035×10^{-6}	—	3	0.5	0.962	—	0.905	0.858
Sun-Venus	2.4478×10^{-6}	—	3	0.5	—	1.039	1.117	1.187
Sun-Venus*	2.4478×10^{-6}	0.723	3	0.5	—	0.751	0.807	0.858

average trajectory experienced between the manifold and switching orbits. The Sun-Earth reference orbit's semimajor axis is therefore $\bar{a} = 0.905$ AU. In the Sun-Venus system, the reference orbit has the semimajor axis $\bar{a} = 1.117 = 0.807$ AU. Similarly to the switching orbit, each reference orbit's eccentricity follows from (2.12) with $C_J = 3$. These parameters (excluding the eccentricities) are neatly summarized above in Table 4.1.

By (3.8), the Earth's chaotic zone has an extent of $r_{\text{RIC}} \sim 3.237 \times 10^{-2}$ AU. Performing this same calculation, but now using orbital elements of the switching orbit, one obtains $r_{\text{switch}} = 2.250 \times 10^{-2} < r_{\text{RIC}}$. The switching orbit is thus contained within the chaotic zone (as is the reference orbit since C_J is admissible) and, therefore, reachable from the manifold orbits. Due to similarity of the two mass parameters and expected approximate symmetry between the interior and exterior RICs, such a transit in the Sun-Venus system should also be (indeed, is) possible. Alternatively, one could check that the RIC is not between Earth (also Venus) and the switching orbit on the energy surface.

4.4.2 Results

Computations were performed over a set of 494×10^6 pairs of initial conditions (ω_0, K_0) scattered about the reference orbit in each system with $(\omega_0, a_0) \in (-\pi, \pi) \times (\bar{a} - 0.01, \bar{a} + 0.01)$,

Table 4.2: A sample set of initial conditions in the Sun-Earth and Sun-Venus systems that resulted in transfer between the two bodies.

System	ω_0	K_0
Sun-Earth	1.384 356 764 533 00	−0.554 484 685 404 083
Sun-Venus	2.461 864 944 055 54	−0.616 944 544 206 183
Sun-Venus*	2.461 864 944 055 54	−0.446 050 905 461 070

where the energy K_0 is given by (2.9), and appropriately iterated 250 times towards the switching orbit. From these initial conditions, 32 295 connection trajectories were successfully established within $\delta = 0.003$ energy units of the switching orbit. These pairs were then used as the set of initial conditions to be iterated towards the manifold orbits; 49 transfer trajectories — coincidentally 10^{-7} as many that was started with — were identified. These transfers were further narrowed by seeking those that made it to within an energy distance of $\delta = 0.001$ and then sorted by time of flight in accordance with (4.7). The initial conditions resulting in one transfer are found above in Table 4.2; its total time of flight is 1391 years.

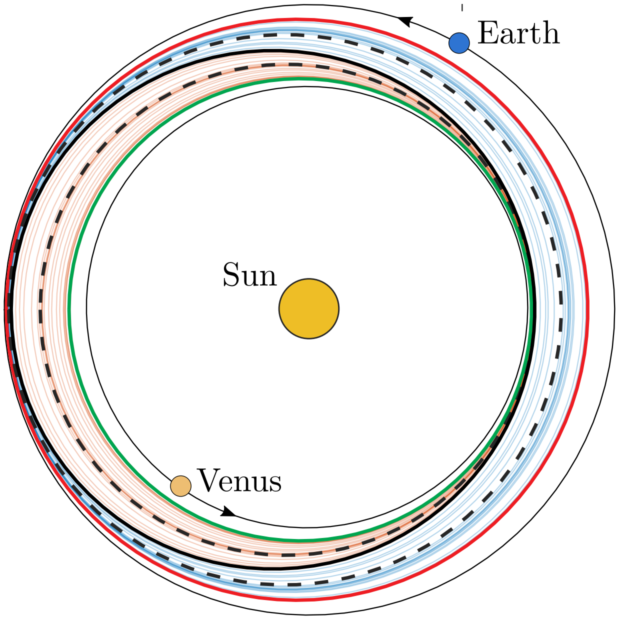

Figure 4.6: An example of an unpowered transfer trajectory with $C_J = 3$ from Earth to Venus. Every 50th orbit is drawn. The blue trajectories represents the particle in the Sun-Earth system, and the orange trajectories for the Sun-Venus system.

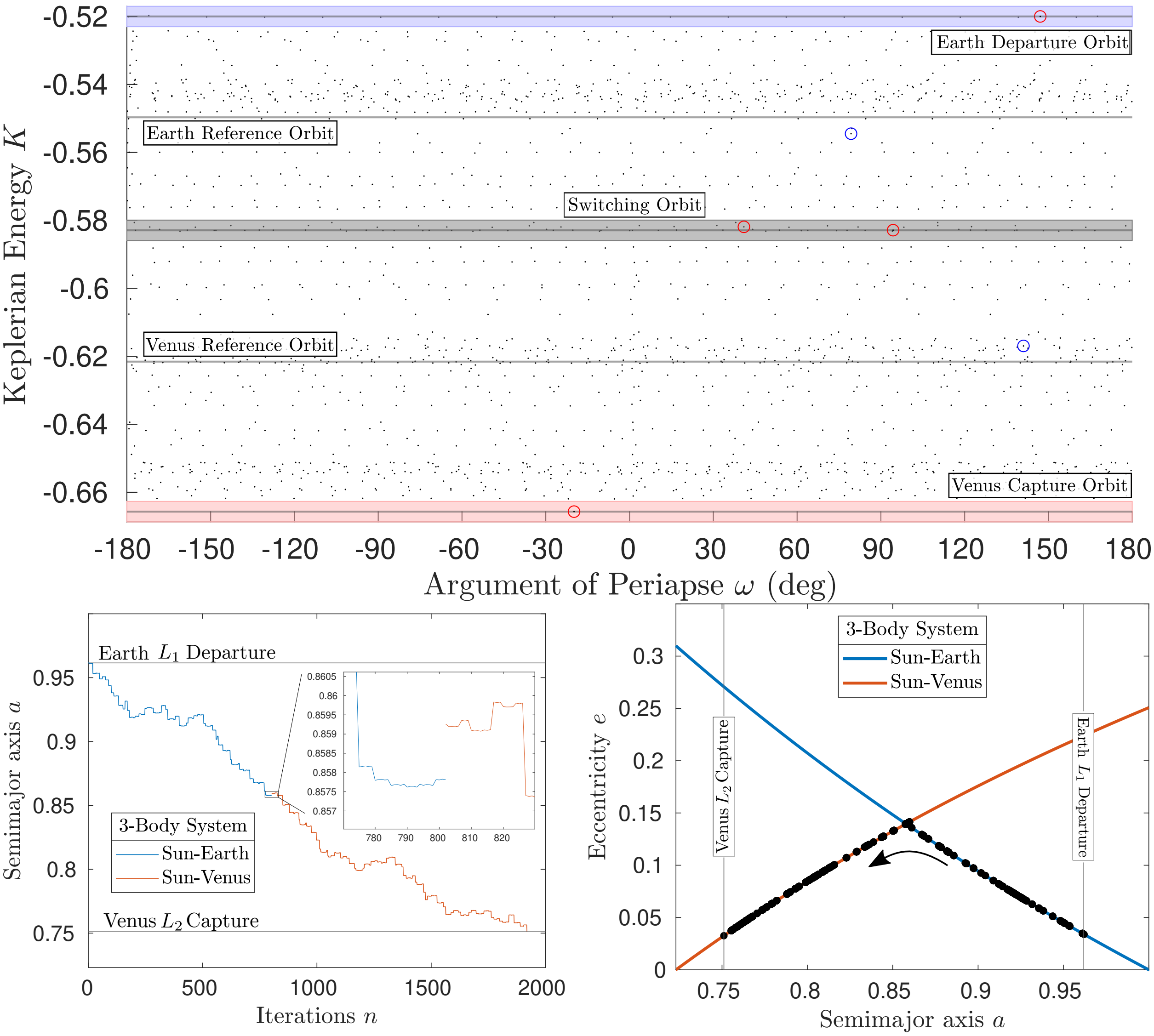

Figure 4.7: Continuation of the example trajectory shown in Figure 4.6. **Top:** Iterates of the initial conditions (circled in blue) in both Sun-Earth and Sun-Venus systems. The transfer is understood to occur in forward time (actually beginning at Earth and arriving at Venus), so the (forward) map $\mathbf{F}$ is used to traverse downwards in a and the inverse map $\mathbf{F}^{-1}$ upwards in a in each system. The motion in the Sun-Earth system is interior; the motion in the Sun-Venus system is exterior. Note that the two systems are plotted together on the same ω axis, but the two planets phase differently. Hence, one needs only check for proximity in K near the switching orbit. (Even if the trajectories don't align exactly in the switching region, continuity dictates that there exist trajectories that do.) **Left:** Evolution of the semimajor axis as viewed from the initial condition starting in the Earth's L_1 manifold orbit. This transfer, which is not optimized, takes 1391 years in total. **Right:** The particle moves along the energy surface provided by the Tisserand parameter.

Chapter 5

Conclusions

Analyzing the phase space of the planar concentric circular restricted 4-body problem (PCCR4BP) is challenging due to its high dimensionality. However, the analysis can be simplified by using a reduced order model under assumptions that the problem is patched together with planar circular restricted 3-body problems (PCR3BPs) and that the motion of the particle is mostly Keplerian. Such simplifications lead to the Keplerian map, a measure of the particle's motion in discrete time using a 2D phase space consisting of its argument of periapse and energy.

From this map, a new estimate of the chaotic zone about the secondary is established by means of rotational invariant circles (RICs). This chaotic zone estimate far exceeds the sphere of influence (SOI)/Hill estimates and is in close agreement with that of Wisdom. The main distinction between this estimate and Wisdom's is that eccentric orbits (and hence the chaotic zone) are characterized along the energy surface provided by the Tisserand parameter instead of entirely circular orbits.

Further, the map is capable of rapidly searching through the phase space and producing trajectories that transfer between the two systems via passive dynamics of gravity assists. This approach is beneficial because it offers large time savings in identifying phase space regions prone to admit transfers over blindly searching with numerical integration and differential correction. Such initial conditions resulting in transfers found by the Keplerian map can then be used as initial guesses in finding the transfer in continuous time.

Bibliography

[1] R. R. Bate, D. D. Mueller, and J. E. White. *Fundamentals of Astrodynamics*. Dover, New York, 1971.

[2] E. Gawlik, J. Marsden, and P. Du Toit. Variational integrators and the three-body problem. *Caltech SURF, Final Report*, 2006.

[3] P. Grover and S. D. Ross. Designing trajectories in a planet-moon environment using the controlled Keplerian map. *Journal of Guidance, Control and Dynamics*, 32:436–443, 2009. doi: DOI:10.2514/1.38320.

[4] M. Guzzo and E. Lega. Theory and applications of fast lyapunov indicators for the computation of transit orbits in the three-body problem. 2021.

[5] W. S. Koon, M. W. Lo, J. E. Marsden, and S. D. Ross. *Dynamical Systems, the Three-Body Problem and Space Mission Design*. Marsden Books, ISBN 978-0-615-24095-4, 2011.

[6] L. Lan and R. Malhotra. Neptune's resonances in the scattered disk. *Celestial Mechanics and Dynamical Astronomy*, 131(8):1–26, 2019.

[7] M. Lecar, F. A. Franklin, M. J. Holman, and N. W. Murray. Chaos in the solar system. *Annual Review of Astronomy and Astrophysics*, 39(1):581–631, 2001.

[8] E. Lega, M. Guzzo, and C. Froeschlé. Theory and applications of the fast lyapunov indicator (fli) method. In *Chaos Detection and Predictability*, pages 35–54. Springer, 2016.

[9] J. Llibre, R. Martinez, and C. Simó. Transversality of the invariant manifolds associated to the Lyapunov family of periodic orbits near L2 in the restricted three-body problem. *J. Diff. Eqns.*, 58:104–156, 1985.

[10] R. Malhotra. Nonlinear resonances in the solar system. *Physica D: Nonlinear Phenomena*, 77(1-3):289–304, 1994.

[11] R. McGehee. *Some homoclinic orbits for the restricted three-body problem.* PhD thesis, University of Wisconsin, Madison, 1969.

[12] J. Meiss. Symplectic maps, variational principles, and transport. *Reviews of Modern Physics*, 64(3):795, 1992.

[13] C. D. Murray and S. F. Dermott. *Solar System Dynamics.* Cambridge University Press, 1999.

[14] A. J. Mustill and M. C. Wyatt. Dependence of a planet's chaotic zone on particle eccentricity: the shape of debris disc inner edges. *Mon. Not. Roy. Astron. Soc.*, 419: 3074, 2012. doi: 10.1111/j.1365-2966.2011.19948.x.

[15] S. D. Ross and D. J. Scheeres. Multiple gravity assists, capture, and escape in the restricted three-body problem. *SIAM Journal on Applied Dynamical Systems*, 6(3): 576–596, 2007.

[16] S. H. Strogatz. *Nonlinear dynamics and chaos: with applications to physics, biology, chemistry, and engineering.* CRC press, 2018.

[17] V. Szebehely. *Theory of Orbits: The Restricted Problem of Three Bodies.* Academic, New York, 1967.

[18] N. Todorović, D. Wu, and A. J. Rosengren. The arches of chaos in the solar system. *Science advances*, 6(48):eabd1313, 2020.

[19] S. Wiggins. *Introduction to Applied Nonlinear Dynamical Systems and Chaos*, volume 2 of *Texts in Applied Mathematics Science*. Springer-Verlag, Berlin, 1990.

[20] J. Wisdom. The resonance overlap criterion and the onset of stochastic behavior in the restricted three-body. *Astron. J.*, 85:1122–1133, 1980.

Appendices

Appendix A

Transformation to Delaunay Variables for Orbital Elements

Given a set of velocity coordinates $(x, y, \dot{x}, \dot{y}) \in \mathbb{R}^4$, information about the trajectory's orbital elements (a, e) can be realized via a time-independent transformation into Delaunay variables $(L, G, l, \bar{g}) \in \mathbb{R} \times \mathbb{R} \times S^1 \times S^1$. The transformation is given by Koon et al. [5], Szebehely [17] and is done by first converting into polar coordinates.

$$\begin{aligned} r &= \sqrt{x^2 + y^2} & G &= r^2(1 + \dot{\theta}) \\ \theta &= \tan^{-1}(y, x) & L &= \frac{r}{\sqrt{2r - r^2\dot{r}^2 - G^2}} \\ \dot{r} &= \frac{x\dot{x} + y\dot{y}}{r} & \bar{g} &= \theta - \cos^{-1}\left(\frac{G^2 - r}{re}\right) \\ \dot{\theta} &= \frac{x\dot{y} - y\dot{x}}{r^2} & l &= \cos^{-1}\left(\frac{a - r}{ae}\right) - \frac{r\dot{r}}{L} \end{aligned} \tag{A.1}$$

Particularly, (2.10) provides the osculating elements $a = L^2$ and $e = \sqrt{1 - G^2/L^2}$. This fully defines the geometry of the trajectory; its orientation is given by the argument of periapse in the inertial frame, $g = \bar{g} + t$. The mean anomaly l relates to the true anomaly via Kepler's equation.